Department of Physics and Astronomy
Heidelberg University

Bachelor Thesis in Physics
submitted by

Dominic Hache

born in Rosenheim (Germany)

2024

Measuring and modelling the ionization and dissociation of methane in a miniature electron beam ion trap at low energies

This Bachelor Thesis has been carried out by Dominic Hache at the
Max-Planck-Institut für Kernphysik in Heidelberg
under the supervision of
Apl. Prof. Dr. José R. Crespo López-Urrutia

Abstract

Miniature electron beam ion traps (EBIT) are conventionally used for the production of highly charged atomic ions. This work presents the first study of molecular ions produced in an EBIT at energies below 80 eV with a particular focus on methane.
To interpret the data of the molecules, we model the behaviour of ion populations by numerically solving a set of coupled differential equations that describe how they increase and decrease, using the runge-kutta method.
Optimal experimental parameters for the production and extraction of molecular ions are measured and subsequently explained by this model. These parameters are then used to measure the ion populations in the trap as the electron beam energy is varied. This provides insight into how methane is ionized/dissociated in the EBIT and how different ion populations are coupled to each other.
An EBIT that is operated at low energies could prove to be a novel source of molecular ions for use in future experiments.

Zusammenfassung

Miniatur-Elektronenstrahl-Ionenfallen(EBIT) werden üblicherweise für die Erzeugung hochgeladener atomarer Ionen verwendet. In dieser Arbeit werden erste Untersuchungen über die Produktion von molekularen Ionen in einer EBIT präsentiert. Diese werden bei Energien unter 80 eV durchgeführt, wobei der Schwerpunkt auf Methan liegt.
Um die Daten von Molekülen zu interpretieren, wird das Verhalten von Ionenpopulationen durch numerische Lösung mehrerer gekoppelter Differentialgleichungen unter Verwendung der Runge-Kutta-Methode modelliert.
Optimale experimentelle Parameter für die Produktion und Extraktion von Molekülionen werden gemessen und anschließend durch dieses Modell erklärt. Diese Parameter werden verwendet, um die Ionenpopulationen in der Falle zu messen, während die Energie des Elektronenstrahls variiert wird. Dies gibt Aufschluss darüber, wie Methan in einer EBIT ionisiert/dissoziiert wird und wie die verschiedenen Ionenpopulationen aneinander gekoppelt sind.
Eine EBIT, die bei niedrigen Energien betrieben wird, könnte sich als neuartige Quelle für molekulare Ionen erweisen, die in zukünftigen Experimenten eingesetzt werden kann.

Contents

1 Introduction

An ion is an electrically charged atom or molecule due to a deficiency or excess of electrons.
Most of the baryonic matter present in the Universe in stars, galaxies and the intergalactic medium is found in highly ionised states [22, 7].
These ions have many transitions in the X-ray regime and have been studied extensively by astrophysical observations [23,24,25].
To improve theoretical models of the formation and behaviour of these astrophysical structures, and to understand observations of them, it is necessary to study the properties of the ions they are composed of. This can be done in the laboratory by producing ions and studying their transitions using X-ray sources.
A well-established ion source for this type of experiment is an electron beam ion trap (EBIT). It uses an electron beam to ionize neutral atoms and trap them. In the experiment, we used a miniature EBIT. It differs from conventional EBITs in that it is designed to take up as little space as possible whilst still providing a good ion trap. This is achieved by using permanent magnets instead of superconducting magnets, which are heavier and take up more space [7].
They lose some of their ionisation capability but gain the advantage of being easily transportable. This allows the mini EBIT to be transported to different X-ray sources such as synchrotrons or free-electron lasers [10].
Typically, miniature EBITs are used to ionize atoms above an energy of 400 eV, which is too high to ionize molecules without completely dissociating them.
While preparing the POLAR-X EBIT[7] for an upcoming beamtime at the ELETTRA synchrotron in Trieste, Italy, we attempted to produce low ionization states of oxygen, nitrogen and carbon at energies below 100 eV. This resulted in the discovery that it is feasible to ionize molecules in the EBIT without completely dissociating them.
The EBIT, operating at low energies, has the potential to be a valuable source of ionized molecules to facilitate studies in the laboratory.
For example, there is some evidence that ionized polycyclic aromatic hydrocarbons are present in the interstellar medium [26]. To test this hypothesis, the visible and infrared spectra of these molecules need to be measured. To do this, the ions need to be produced and cooled. The EBIT could be used to produce these ions.
It also may be interesting to study the interaction of ionized molecules with different light sources like synchrotron radiation.
In this thesis, we want to establish a foundation to comprehend the ionization and dissociation processes of molecules inside the EBIT, as well as the behavior of the experiment at low energies. Our focus will be on methane molecules.
The primary technique for assessing the ion content of the trap in this thesis is to extract the ions from the trap and measure their time-of-flight (TOF) to determine their charge-to-mass ratio.
We will investigate the optimal trapping and extraction parameters such as trap depth, gas pressure and time of interaction with the electron beam. This will help us to understand how best to study the molecules and maximize the signal strength.
The energy of the electron beam is varied to study its effect on the ion populations. A TOF spectrum of ethane is measured to see what kind of dissociation and ionization is possible in a molecule different from methane.
A closer look will be taken at methane, where we will study how different ion populations influence each other.

To better interpret the data we model the behaviour of the ions by numerically solving a set of coupled differential equations that describe the rate of change of the individual populations, using the runge-kutta method.
The work is divided into four parts. In the first part we will present the theory necessary to understand the processes in the EBIT. The second part explains the experimental setup. We then describe how the measurements were made and discuss the influence of various sources of error on the accuracy of our results. After the physics and measurements are described we discuss the modelling of the ion populations. Finally, we will analyse and interpret the data.

2 Theory

In order to better understand the experiment and the interpretation of the data collected in this thesis, it is necessary to discuss the underlying physics of the EBIT, as well as the physics of the ionization and dissociation of methane.
It should be noted that there are many more processes in the EBIT than we have listed here. In particular, we won't discuss processes related to the absorption of photons, as these are not relevant to our measurements.
Instead, we will concentrate mainly on electron-ion interactions.

2.1 Ions

The most fundamental function of an EBIT is to trap and produce ions. The mechanism that the EBIT uses for this leads to positively charged ions.
We now discuss the different mechanisms that lead to ionization.

2.1.1 Direct ionization

Direct ionization may occur when the kinetic energy of a colliding electron from the continuum is above the binding energy of an electron in an atom.
The bound electron is then removed from the potential of the atom via an inelastic collision. This process is called electron impact ionization.[18]
This is the process by which atoms and molecules are ionized inside the EBIT:

$$\mathrm{A}^{+q} + e^- \rightarrow \mathrm{A}^{+(q+1)} + 2e^- \tag{1}$$

Where A denotes an atom, q is its charge and e^- is an electron.
When an electron is removed from an atom the remaining electrons are more tightly bound. Because of this the energy that is needed for further ionization rises with the number of expelled electrons.

Cross section of direct ionization

The cross section is a measure for the likelihood of a process occurring. As the present experiment varies the energy it is important to understand the cross section's dependence on the energy.
An attempt at describing the energy dependence of the ionization cross section was made by Wolfgang Lotz in the form of an empirical formula [2].
It assumes that the total cross section of the ionization is a sum of the individual ionization cross section of all the electrons in the atomic orbitals. The cross section of the removal of electrons at the same energy level are equal. At the i-th energy level the cross section for ionization is described by:

$$\sigma_i = a_i q_i \frac{\ln(E/P_i)}{E P_i}[1 - b_i \exp\left(-c_i \frac{E}{P_i} - 1\right)] \tag{2}$$

where a_i, b_i, c_i are parameters that have to be determined experimentally, P_i is the binding energy, E is the kinetic energy of the incoming electron and q_i is the number of electrons in the i-th sub shell.
If the kinetic energy of the incoming electron is smaller than the binding energy $E < P_i$ the cross section is negative and no ionization can take place. When $E > P_i$ ionization is possible and the cross section is unequal to zero.

The cross section reaches its maximum when the kinetic energy of the incoming electron is around two to three times the binding energy. Afterwards it gradually decreases back to zero.

2.1.2 Radiative recombination

Radiative recombination occurs when a free electron is captured by the potential of an ionized atom [15]. The free electron is bound to the atom while a photon of the energy of the difference between the energy of the free electron and the binding energy of the atom is emitted:

$$\mathrm{A}^{+(q_i)} + e^- \rightarrow \mathrm{A}^{+(q_i-1)} + \hbar\omega \tag{3}$$

where q_i is the charge of the ion, $\hbar$ is the reduced planck constant and ω is the frequency of the emitted photon. The energy of the photon can be calculated by taking the difference of the kinetic energy of the free electron E_{kin} and the binding energy of the ion E_B:

$$E_{Ph} = \hbar\omega = E_{kin} + E_B \tag{4}$$

The cross section for this process is given by[31]:

$$\sigma_{RR} = \frac{32\pi a_0^2 \alpha^3}{3\sqrt{3}} \frac{Z|E_0|^{3/2}}{(E_0 + E)E} \tag{5}$$

with

$$E_0 = Z^2 R_y / n^2 \tag{6}$$

where a_0 is the Bohr radius, α is the fine structure constant, n is the principal quantum number.

2.2 Molecules

Molecules are composed of atoms that are chemically bound to one another.
In this work we will consider the molecules methane(CH_4) and ethane(C_2H_6). They belong to the chemical class of alkanes[3]. Alkanes are a class of organic molecules that are made up of hydrogen and carbon atoms where only single bonds are present between atoms. They are referred to as saturated hydrocarbons, as they have the maximum number of hydrogen atoms per carbon due to the single bonds in the molecules. Their structure can generally be written as C_nH_{2n+2} where n is a natural number.
We lay a special focus on methane as there is good literature available describing the behaviour of methane when interacting with an electron beam. [4, 5, 6]
Methane and ethane are widely available in gaseous form, which makes injecting them into the vacuum chamber of the EBIT easy.

2.2.1 Ionization and dissociation processes of methane

When methane interacts with an electron there are many possible reactions. Most notably there are the processes of ionization and dissociation.
Ionization again refers to the process of removing an electron from the binding potential of a molecule. Dissociation on the other hand refers to the process of a molecule losing one or more atoms from its binding potential.

The processes that can happen in our experiment can be classified into five different reactions. We will now proceed to list all possible reactions between methane or a dissociation product of it CH_y and an electron e [5, 6]:

Electron impact ionization

$$e + \mathrm{CH_y} \rightarrow 2e + \mathrm{A}^+ + \mathrm{B}_1 + \mathrm{B}_2 + ... \tag{7}$$

Here A^+ refers to an atomic or molecular ion, while B_1, B_2 are potential neutral fragments. In this process a neutral molecule is either just ionized without dissociating it or it is dissociated and ionized. This produces neutral fragments in addition to the ionized molecule.
The cross section of this process is given by [5]:

$$\sigma = \frac{10^{-13}}{EI_c}\left[A_1 \ln\left(\frac{E}{I_c}\right) + \sum_{j=2}^{N} A_j \left(1 - \frac{I_c}{E}\right)^{j-1}\right] (\mathrm{cm}^2) \tag{8}$$

where E is the electron beam energy, I_c is the threshold energy and A_j are fitting parameters provided in [5].

Neutral dissociation

$$e + \mathrm{CH}_y \rightarrow e + \mathrm{B}_1 + \mathrm{B}_2 + ... \tag{9}$$

A neutral molecule is dissociated to multiple lighter molecules/atoms without any ionization occurring.
The cross section for this process can be modeled by [5]:

$$\sigma = 34.6(1 + 0.29y)\left(1 - \frac{I_c}{E}\right)^3 \frac{1}{E}\ln(e + 0.15E)(10^{-16}\mathrm{cm}^2) \tag{10}$$

where y is the number of hydrogen atoms in the alkane that is dissociated, e is Euler's number.

Dissociative excitation

$$e + \mathrm{CH}_y^+ \rightarrow 2e + \mathrm{A}_1^+ + \mathrm{B}_1 + \mathrm{B}_2 + ... \tag{11}$$

Here an already ionized molecule CH_y^+ dissociates into one ionic fragment A_1^+ and multiple neutral fragments. The cross section of this process can be similarly modeled by [5]:

$$\sigma = 29.4(1 + 0.71(y - 1)\left(1 - \frac{I_c}{E}\right)^{2.5} \frac{1}{E}\ln(e + 0.9E)(10^{-16}\mathrm{cm}^2) \tag{12}$$

Dissociative ionization

$$e + \mathrm{CH}_y^+ \rightarrow 2e + \mathrm{A}_1^+ + \mathrm{A}_2^+ + \mathrm{B}_1 + \mathrm{B}_2 + ... \tag{13}$$

This is very similar to the process of dissociative excitation but rather here two ionized fragments are produced. This class of processes also have a larger appearance energy than dissociative excitation.
The cross section here is given by [5]:

$$\sigma = 30.1(1 + 0.086(y - 1)\left(1 - \frac{I_c}{E}\right)^{1.55} \frac{1}{E}\ln(e + 0.5E)(10^{-16}\mathrm{cm}^2) \tag{14}$$

Dissociative recombination

$$e + \mathrm{CH}_y^+ \rightarrow \mathrm{B}_1 + \mathrm{B}_2 + ... \tag{15}$$

Here a molecular ion is dissociated into neutral fragments.
The cross section for these kinds of processes can be approximated by:

$$\sigma = \frac{A}{E^\alpha (1 + aE)^\beta} (10^{-16} cm^2) \tag{16}$$

with fitting parameters A, a, α, β.
A full list with all the fitting parameters to calculate the cross sections may be found in [5].
In Figure 1 we show a graph of the cross section of the ionization of neutral methane. The cross section is negative before the appearance energy of 12.6 eV. The small increase before this energy is surpassed is non physical and is a consequence of shape the fitting function. It rises until around 70 eV where it reaches its maximum and then slowly starts to decline.

Other cross sections have a other shapes and reach their maximum at different energies. We will not show every cross section here.

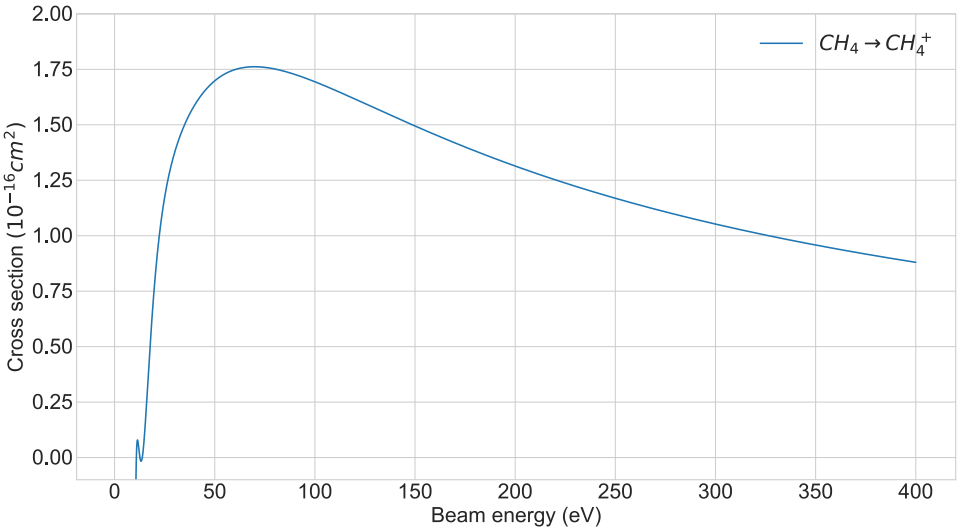

Figure 1: Cross section of the ionization of neutral methane. The behaviour before the appearance energy of 12.6 eV is unphysical and due to the formula of the empirical fit.

3 Experimental setup

This section discusses the experimental set up, including the individual parts of an EBIT, the process for the time-of-flight measurement, and the electronics used for signal reading.

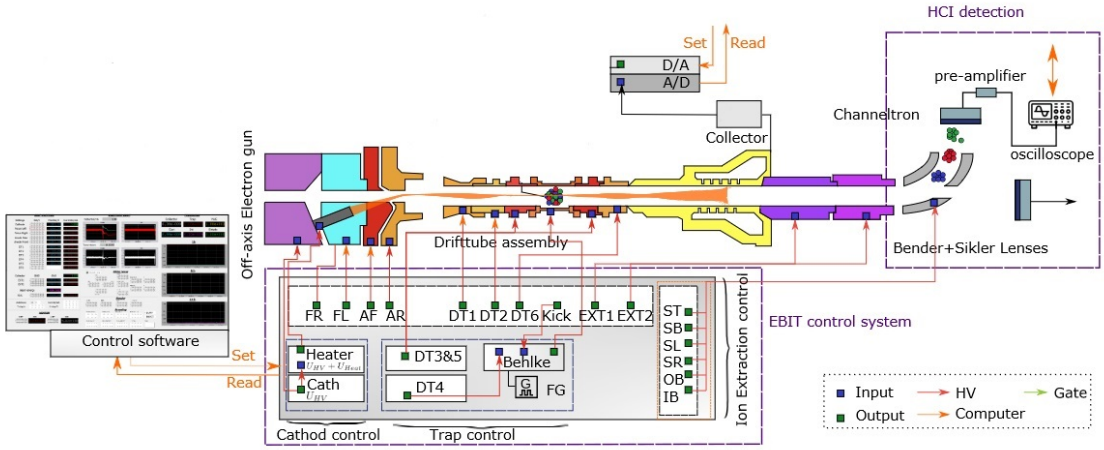

Figure 2: Scheme experimental setup. EBIT in the center with the beam line, readout electronics and oscilloscope at the right end, below the EBIT the power supplies, on the left hand side user interface of the control software. Adopted and modified from [10]

3.1 PolarX-EBIT

An electron beam ion trap (EBIT) is used to produce and study ions. The process involves directing an electron beam at a cloud of neutral atoms to ionise them. The ions are then trapped radially by the negative space charge of the electron beam and axially by a potential well created by three cylindrical electrode
The POLAR-X EBIT is a specific model of EBIT that was developed at the Max Planck Institute for Nuclear Physics. It is a more compact version of the traditional EBIT, which typically uses superconducting magnets to generate a magnetic field. However, the POLAR-X EBIT uses smaller permanent magnets, making it easier to transport.[8] The equipment is also fitted with an off-axis electron gun, which is beneficial for the use of synchrotron radiation.[10]. The EBIT has many individual parts that must be understood in order to make sense of the experimental parameters we will use to describe the measurements.

3.2 Drift tubes

The drift tubes are used to guide the electron beam and create an axial trapping potential to confine the ions.
In total there are six cylindrical electrodes, each of which can be set to an electrical potential. They are numbered from one to six. The drift tubes are connected to power supplies that can change the electronic potential of the drift tubes in a range from 1 V to about 3 kV. This increases the transmission T.
This transmission T refers to the ratio of the current leaving the cathode to the current reaching the collector.

$$T = \frac{I_{collector}}{I_{current}} \tag{17}$$

This is an important measure for this experiment as it describes how efficiently the electrons are guided from the cathode to the trap centre. A high transmission means that more electrons enter the trap centre, leading to a higher probability of interaction between electrons and atoms. The three central drift tubes are used to provide axial confinement of the charged particles.
A common way of trapping ions is the symmetrical trap. This involves setting DT3 and DT5 at the same potential, which is higher than that of DT4 at the centre of the trap. To move a charged particle beyond the potential of DT3 or DT5, work must be done. This results in particles of sufficiently low kinetic energy being trapped axially by the potential well.

3.3 Magnetic field

To achieve a high number of trapped ions, high current densities in the trap centre are aimed for. This results in a higher number of electrons that can potentially interact with the atoms/ions, increasing the probability of ionisation.
An assembly of magnets is used to compress the electron beam at the centre of the trap, increasing the current density.
The geometry of the magnetic field is chosen so that the magnetic flux density at the trap centre is maximal at about 0.8T[7] and zero at the cathode and collector positions. This results in maximum compression at the trap centre.

3.4 Electron beam

The electron beam is used to ionize and trap ions, making it essential to the experiment.

3.4.1 Electron gun

The electron beam is generated by the electron gun. It consists of a barium-impregnated tungsten cathode which is heated until its electrons escape from the metal by thermionic emission [7]. The electrons are then accelerated by electrodes towards the centre of the trap, where they ionise a cloud of atoms.
The electron gun used in POLAR-X is positioned off-axis, i.e. at an angle to the x-direction of the experiment, as shown in figure 3. This geometry is beneficial for many spectroscopy experiments because it allows for the use of a laser beam parallel to the electron beam.
This is a disadvantage for the specific experiment we are conducting, as the electron beam has to be bent at an angle before it is in line with the target. This causes current loss at different parts of the electron gun, specifically the rear anode, which reduces the number of ions produced in the trap. Additionally, this setup requires more electrodes to guide the trajectory of the electron beam, resulting in more parameters to optimize compared to the on-axis gun setup. To bend the beam correctly, the electron gun utilises four electrode: focus left, focus right, anode back and anode front.
As previously stated, the experiment aims to minimise the Lorentz force by keeping the magnetic flux at the cathode as close to zero as possible. However, this is not feasible in practice. Therefore, we need to adjust the left and right focus electrodes

to compensate for the slight Lorentz force acting on the electrons by directing the beam left and right.
The electrons are accelerated away from the cathode by the rear anode, while the front anode bends them around the angle.

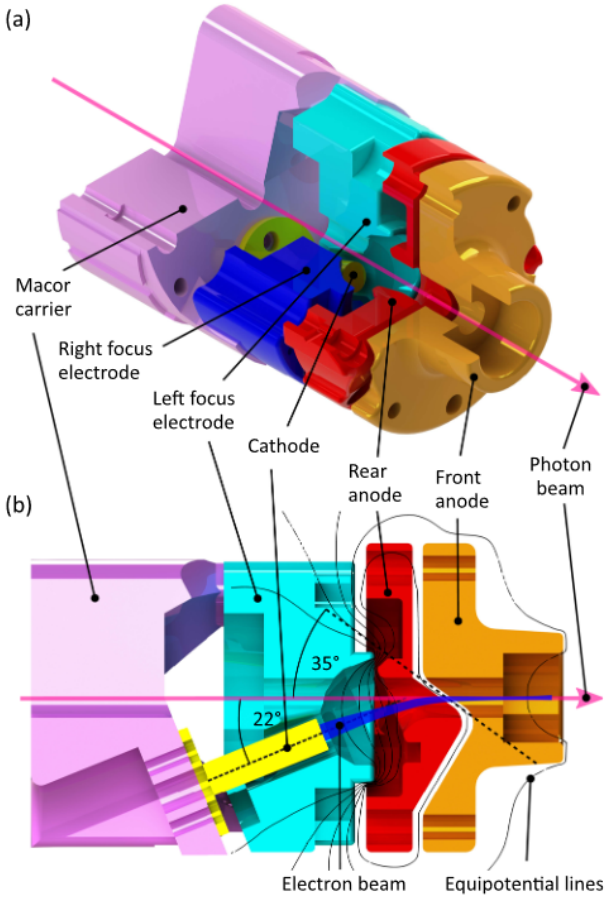

Figure 3: Off-axis electron gun. Different colors: focus right (dark blue), focus left (turquoise), cathode (yellow), anode rear (red) and anode front (orange). Bending of the electron beam in (b) as well as the insertion of a photon beam in (a) and (b). Adopted from [7]

In addition to the electrodes, the transmission of the electron beam can be improved by adjusting the gun position. Three manipulators are used for the x, y and z positions to change the initial position of the electron beam, which can be helpful in guiding it. The spatial extent of the electron beam is a crucial parameter, as it determines the number of ions that can be excited and trapped based on the area enclosed by the current and the current density within
The Hermann radius r_H [9] is a useful measure of the spatial extent of the electron beam. Within this radius 80% of the electron beam current I_b can be found:

$$r_H = r_B \sqrt{\frac{1}{2} + \sqrt{\frac{1}{4} + \frac{8 m_e k_B T_C r_c^2}{e^2 B^2 r_B^4} + \frac{B_C^2 r_c^4}{B^2 r_B^4}}} \tag{18}$$

where r_c is the cathode radius, T_C is the cathode temperature, B_C is the magnetic field strength at the cathode, m_e is the electron mass, e the elementary charge, k_B is the Boltzmann constant, B is the magnetic field strength at the trap and r_B is the Brillouin radius:

$$r_B = \sqrt{\frac{2 m_e I_b}{\pi \epsilon_0 v_z e B^2}} \tag{19}$$

with v_z the electron velocity and ϵ_0 the vacuum permittivity.
The space charge $\Phi_e(r)$ provided by the electron beam, if one assumes a cylinder of constant density with a radius r_e, is [10]:

$$\Phi_e(r) = \frac{I_b}{4\pi\epsilon_0 v_z}\left(\frac{r^2}{r_e^2} + \ln(\frac{r_e^2}{r_D^2}) - 1\right) \tag{20}$$

for $r \leq r_e$ and

$$\Phi_e(r) = \frac{I_b}{4\pi\epsilon_0 v_z}\ln\left(\frac{r^2}{r_D^2}\right) \tag{21}$$

for $r \geq r_e$. Here r_D is the inner radius of the drift tubes.
It can be seen that the only spatial dependence of this potential is the radial distance from the beam r. This negative potential is used to trap positive particles. Because of the radial dependence of this potential, a charged particle can be moved along the beam at a constant radius without changing the potential. However, if a particle's radial distance from the beam is changed, work must be done.
In conclusion this potential traps ionized particles radially but not axially. The axial trapping will be described in section 3.2.

3.4.2 Space charge

It is important to consider the electrostatic effects that ionized particles have on the experiment.
When ions are present in the trap they provide a space charge Φ_i. The total space charge Φ_{tot} experienced by the electrons is the sum of the space charge from the electron beam and the space charge from the ions:

$$\Phi_{tot} = \Phi_e + \Phi_i \tag{22}$$

The uncorrected (nominal) electron beam energy is given by the potential of the cathode plus the potential of the central drift tube DT4.
The true beam energy is not the nominal beam energy, but the sum of the cathode potential Φ_c, the potential of DT4 Φ_{DT4} and Φ_{tot}:

$$E_{el} = e(\Phi_c + \Phi_{DT4} + \Phi_e + \Phi_i) \tag{23}$$

This results in an energy shift, so that different ionization states appear at a higher nominal energy than the literature values (which refer to the true electron energy).

3.4.3 Collector

To stop the electron beam at the end of the EBIT, it is directed onto the collector. The collector is a conductor that is grounded and water-cooled. The grounding is necessary to prevent the electrons from accumulating on the collector. When the electrons leave the collector through the grounding, the resulting current heats the collector. Water cooling is installed to prevent it from overheating.
To ensure that the electrons don't pass through the collector, two extractor electrodes are placed at a more negative potential than the cathode, which is located behind the collector.
To determine the electron current at the collector, we measure the voltage across a $1\,\mathrm{k}\Omega$ resistor with the collector connected to ground. Using Ohm's law:

$$I = \frac{U}{R} \tag{24}$$

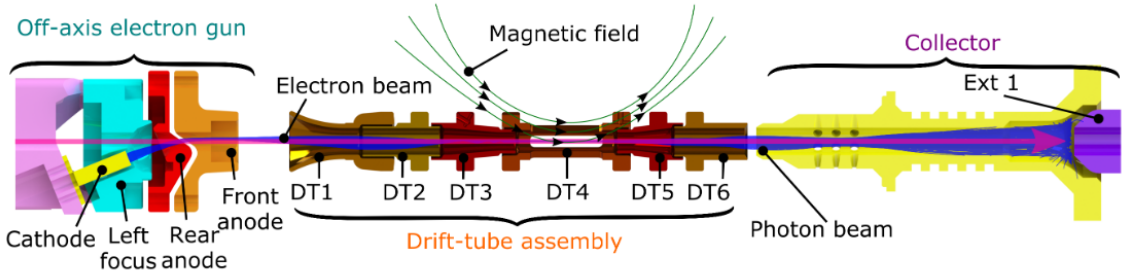

Figure 4: Cathode, drift tubes and collector, off-axis electron gun and drift tubes. Adopted from [7]

where I is the current, U is the voltage and R is the resistance, we can determine how much current is flowing to the collector.
We want to extract the ions later to measure their charge state distribution. We will describe this in section 3.8. To do this, the ions will leave the EBIT in the same way as the electrons. In order to absorb only the electrons and let the ions pass through undisturbed, the collector has a hole in the centre. As the magnetic field at the collector is zero, the electron beam expands and its current density is reduced. As the ions are positively charged, they are attracted by the negative potential of the extractor and can leave the EBIT through the hole in the collector.

3.5 Beamline

Our main method of measuring ions will be to extract them directly from the trap. This is done by applying a high voltage to the central drift tube to accelerate the ions out of the trap (more on this in section 3.8).
A beamline consisting of a Sikler einzel lens and bender electrodes is used to guide the ions[7].
The Sikler lens consists of four electrodes (left, right, top, bottom) to focus the ion beam.
The benders are two electrodes (outer and inner) that bend the ion beam.
If a laser were used for spectroscopy in this experiment, it would be extracted parallel to the axis of symmetry of the drift tubes. If ions were also extracted directly from the trap, both the ions and the laser would be extracted in the same direction, which is impractical.
Instead, it makes sense to extract the ions separately at a 90° angle to avoid problems with the laser. For this reason, the two bender electrodes are used to bend the electron beam to this 90° angle.
The ions are then directed to an electron multiplier which is connected to an oscilloscope to display the TOF spectrum (more on this in the 3.8 section).

3.6 Vacuum system

Ions interact with the neutral gas around them, which reduces extraction efficiency. We want as few uncontrolled interactions of ions with neutral gas atoms as possible. It is therefore necessary to create a high vacuum inside the EBIT.
Furthermore, the cathode will erode if exposed to sufficiently high levels of oxygen. Lastly, if the pressure around the gun is too high, the electrons interact with the gas to form a plasma, which can damage the cathode.

In total, we use six turbomolecular pumps and a scroll pump for pre-vacuum to create a vacuum of the order of 1×10^{-9} mbar inside the chamber.

3.7 Injection system

The injection system enables the injection of various types of atoms/molecules into the trap centre.
The molecules injected are all gaseous, which facilitates the injection process.
A small volume, separated from a larger volume, is filled with gas at pressures of up to 6 bar. A needle valve removes the separation between the two volumes and the gas begins to fill the second volume.
Two slits in this section create a stable particle beam into the centre of the trap. This enables very precise changes in trap pressure.

3.8 Time-of-flight measurement

At the energies at which we operate the EBIT, it is not possible to measure a photon signal with the SDD installed on the EBIT. At these low energies, the wavelength of the photons is too long.
Instead, we opt for a time-of-flight (TOF) measurement to identify the ions and their population size.
In a TOF measurement we exploit the fact that different ions have different ratios of charge q to mass m, q/m. We will use this by accelerating the ions in an electric field and measuring the different times it takes the ions to travel a certain distance to measure the q/m ratio.
A sudden increase in voltage across the central drift tube (the kick) can be used to extract the ions from the trap and accelerate them towards an electron multiplier. In addition to the kick potential, the ions also experience the potential of the extraction electronics, giving the total extraction potential:

$$U_{tot} = U_{\text{extraction}} + U_{kick} \tag{25}$$

The kinetic energy that the ions acquire by this is proportional to the extraction potential and the charge q of the ions:

$$E_{el} = qU_{tot} \tag{26a}$$

the velocity of the ions can then be calculated by:

$$E_{kin} = \frac{1}{2}mv^2 \tag{26b}$$

use $E_{el} = E_{kin}$ and rearrange for v:

$$v = \sqrt{\frac{2qU_{tot}}{m}} \tag{26c}$$

The time t it takes the ions to traverse the distance Δx to the electron multiplier is:

$$t = \frac{\Delta x}{v} = \frac{\Delta x}{\sqrt{2U_{tot}}} \frac{1}{\sqrt{\left(\frac{q}{m}\right)}} \tag{26d}$$

This last equation 26d is only valid because the acceleration time is short, so that the ions travel most of the way at a constant speed. This is the case because the applied fields are of sufficiently high intensity.

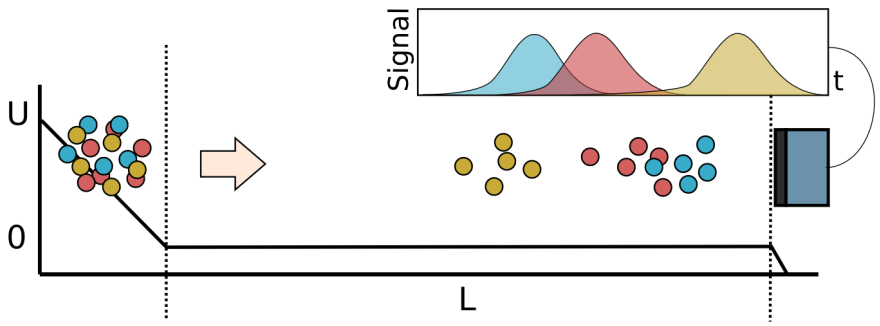

Figure 5: Scheme of the time-of-flight measurement. Colors indicate ions with different q/m ratios. Indicated is the resulting signal from the difference in time of flight to traverse the length L. Adopted from [1]

It can be seen that the TOF of the ions only depends on the q/m, as Δx and U_{tot} are assumed to be the same for all ions.
This assumption is reasonable since the spatial extent of the ion cloud is much smaller than the distance Δx travelled. However, we will see a broadening of the peaks as a result of the spatial extent of the cloud.
There are a number of errors associated with TOF measurements.
The most important effect to consider is that the beam line is optimized for a certain range of q/m values.
In practice, one of the q/m peaks in the TOF signal is optimized to be maximum. The result is that other q/m values are not extracted as well as the q/m we have optimized for. This is easy to see as optimizing another peak will cause a reduction in the peak we optimized first.
We get this effect because the trajectories of charged particles will be slightly different depending on their q/m. Particles with different q/m values will be focused differently in the Sikler lens and bent slightly differently in the bender.
As we will be using the integrated peak intensity as a measure of the relative population of the ion (see section 6.1), this means that it is not entirely possible to give an absolute estimate of the population of an ion, as the extraction efficiency will be different depending on how far the q/m value of the ion is from the ion population we are optimising for.
However, the relative change of a population will still be visible, as the behaviour of the ion trajectory will not usually change with variation of the experimental parameters. It is the relative change of the ion populations that we are mainly interested in.
There is a limit to how wide a time window in the TOF spectrum we can expect to measure with good accuracy and efficiency. In practice, we will see a spectrum that is about 6 μs wide in total, and choose to focus on a slice of that spectrum that is about 1 μs wide.
We optimize a peak that is in the centre of this 1 μs slice. We may not get a direct proportionality between the peak height and the number of ions of that population in the trap due to the inefficiency of the extraction, but we can get a good understanding of the relative change of a given population, which is often what we are more interested in.
This time frame of 1 μs is also sufficiently small that the position of the peaks in time does not change significantly when you change which peak to optimise for.

Another effect to consider is the spatial extent of the cloud inside the trap, which results in slightly different path lengths that the ions have to travel before reaching the electron multiplier. The extent of the cloud is very small compared to the total length travelled by the ions. Given this large difference between the length of the cloud and the extent of the beam line, the travel times are sufficiently different that we can resolve individual peaks, although we still see the spatial extent of the cloud in the width of the peaks (see figure 5).
To generate the kick pulse, we utilise a function generator and a Belkhe high voltage switch. The function generator can produce an electrical signal of a programmable shape. The Belkhe high voltage switch then transforms this low voltage signal into a high voltage signal. We choose a very sharp rise in voltage for a brief period. Ideally, the function would have the shape of a step function, rising infinitely quickly to the chosen peak voltage of the kick and falling back to zero in the same way. In reality, this is not possible. The impulse has a certain build-up time. It is reasonable to assume that many ions will leave the trap before the pulse reaches its maximum intensity. This means that they do not experience the full potential of the kick, and therefore have a different speed at which they cross the beamline than we would expect from the formula above.
This leads to additional scattering of the ion peaks in the time-of-flight spectrum. This is accounted for in the error of the TOF calibration when we consider the standard deviation of the mean for the peaks.
Also, we are not necessarily interested in the flight times per se, but rather in the flight times as a means of determining what type of ions are in the trap, how much of one ion there is compared to another, and how each population changes as different parameters are varied.

3.9 Electronics

A Channeltron is a type of electron multiplier. It is cylindrical in shape and consists of a material that emits secondary electrons when hit by a primary electron. These secondary electrons cause the material to emit more electrons until a large pulse of electrons arrives at the other end of the device. This cascade of electrons only occurs when a high voltage is applied between the back and front of the Channeltron.
The detection efficiency of the channeltron has a certain energy dependence [13]. The ions we will be extracting all experience a similar extraction potential, and as most of them are singly charged, they will have the same kinetic energy with small non-significant deviations due to the velocity distribution:

$$E_{\text{kin}} = q_i U_{\text{tot}} \tag{27}$$

where $U_{\text{extraction}}$ is the extraction potential. Thus the effect of energy on extraction efficiency can be assumed to be negligible.
Some electronics are required to properly generate and measure this signal. The electronic circuit we use is shown below. The function of this circuit and the physical effects on the signal have been well described by Jonas Danisch in [10].
The circuit consists of three resistors and two capacitors.
In order for the secondary electrons to flow from the front of the Channeltron to the back, the back needs to be at a more positive electrical potential than the front. A high voltage (HV) is connected to the front and back of the Channeltron. This is to provide a potential that can be manipulated by the resistors to achieve the desired effect of a potential difference.

The resistors R_1 and R_2 act as voltage dividers and provide this potential difference between the back of the Channeltron and the anode, which is connected to ground. There is also a capacitor C_1 between the HV and ground to prevent an AC voltage from appearing.

Figure 6: Picture of a channeltron. Ions enter through the conical shape on the top. In the curled metal secondary electrons are emitted. Bottom: the connections for the high voltage.

This is the first part of the measurement. The incoming primary electrons are now able to produce secondary electrons due to the potential difference. The resulting signal is a charge pulse.
The charge pulse from the channeltron now charges the capacitor C_2 according to $dU = \frac{dQ}{C}$, which is connected to ground via a resistor R_3. The accumulated charge causes a current pulse I given by $I = \frac{dQ}{dt} = C\frac{dU}{dt}$. After the channeltron pulse, the capacitor discharges through the resistor R_3, behaving like an RC element with $\tau = R_3C_2$. The current is negative and approaches zero exponentially. If the signal is sufficiently narrow in time, it can be described by

$$I(t) = -I_{max}e^{-\frac{t}{\tau}} = -\frac{U}{R_3}e^{-\frac{t}{\tau}} \tag{28}$$

where $U = \frac{Q}{C}$. The current pulse is converted into a voltage pulse that can be interpreted by an oscilloscope after passing through a preamplifier.
As you can see, the amplitude of the current discharge is inversely proportional to the resistance R_3 and the capacitance C_2. In order to obtain a small discharge current, it is necessary to choose large values for these two properties.
On the other hand, the half-life of the current is also proportional to these properties: $T_{\frac{1}{2}} = R_3C_2\ln(2)$.
If the signal consists of many peaks that are close in time, it is necessary to find a good balance between the discharge amplitude and the half-life of the signal. A long half-life will cause subsequent peaks to be within the negative discharge. On the other hand, a large ringdown will dissipate more quickly, but will have a greater effect on the signal strength of the following peaks.
The above discussion shows that the signal is affected by the electronics, specifically by the discharge from C_2.
Due to the spatial extent of the ion cloud, the signal has a Gaussian shape. Two electronic artefacts are connected with this signal: The so-called ringdown and a delayed pulse caused by reflections in the cables.
We will solely discuss the ringdown. The delayed pulse is a consequence of reflections in the cables, but it is not observed in our spectra (and if it is, it is negligible). This may be because we produce so few ions at low energies that the resulting low signal intensity does not produce visible reflections as they are lost due to electronic losses in the cables.
However, we do see ringdowns in the TOF spectra. The ringdown of a peak is a consequence of the negative discharge of the capacitor with capacitance C_2.
It is a valley that is found after each peak, where the extent of the valley depends on the intensity of the preceding peak. As shown in [10], the signal is composed of the

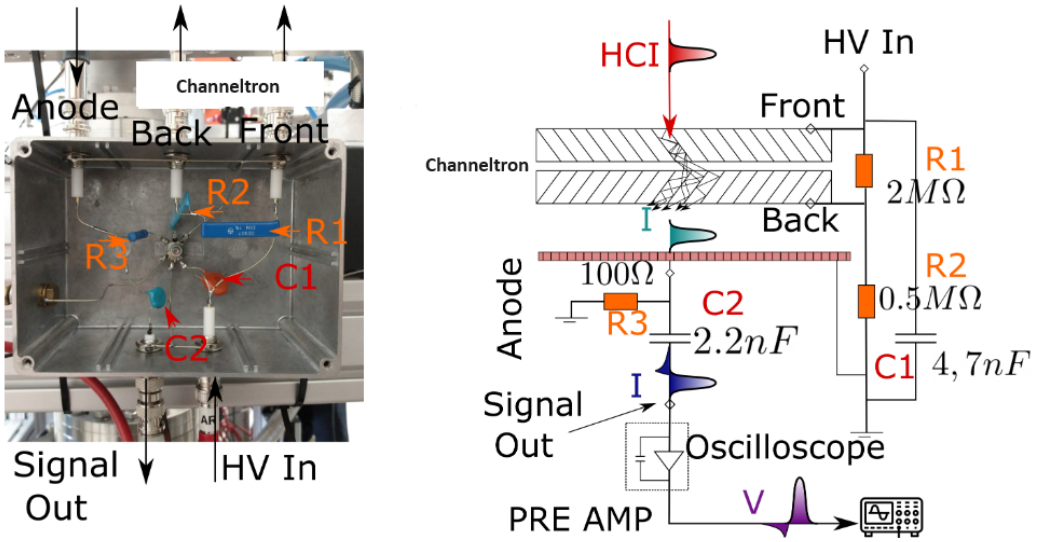

Figure 7: Picture of electronic circuit (left) and schematic of the same circuit (right). Adopted and modified from [10]

peak and the following ringdown. The ringdown can be described as a convolution of a Gaussian curve and an exponential decay:

$$I(y) = e^{-\lambda x} * \frac{1}{\sigma\sqrt{2\pi}} e^{\frac{-x^2}{2\sigma^2}} = \frac{1}{2}\exp(-\lambda(y - \frac{\sigma^2\lambda}{2}))[1 + \text{erf}(\frac{y - \sigma^2\lambda}{\sqrt{2}\sigma})] \tag{29}$$

where $I(y)$ is the ringdown signal, λ is the exponential constant of the decay, σ is the standard deviation of the Gaussian, $*$ indicates a convolution and erf(...) is the error function.
The theoretical signal described in the equation 28 is only true if the signal is very narrow in time. In reality the signal is more like a Gaussian curve, so equation 29 is a better approximation.
To achieve a higher level of accuracy in estimating the population size and how it changes, we will later correct the methane spectra for the ringdowns.
For other measurements it will not be necessary to correct for the ringdown as it is small compared to the peak intensity. The correction made to account for this effect is small and does not affect the conclusions drawn from the results.
More on the exact correction of this effect and when we are correcting for it will be discussed in section 6.6.1.

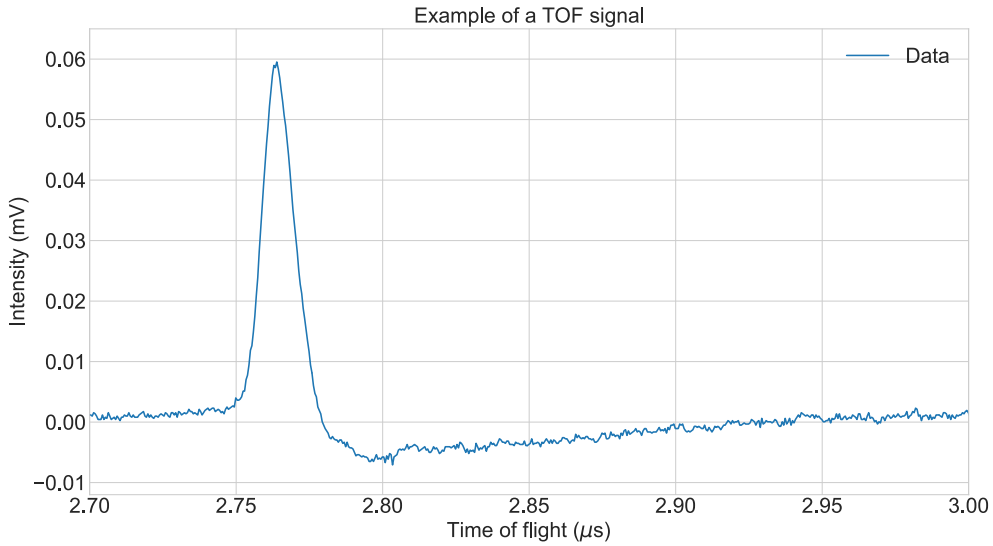

Figure 8: Signal with ringdown from TOF spectrum of ethane. The ringdown is located roughly between 2.78 μs and 2.95 μs where the values of the signal are negative.

4 Data acquisition

In this section we will describe the different measurements, discuss sources of error associated with each measurement, and show some of the data we have obtained. We will also talk about the process leading up to the measurements, how we find good experimental parameters and how we collect the data.

4.1 Low energy parameters

An EBIT is normally operated at energies of $> 100\,\text{eV}$. To reach lower energies, the experimental parameters were slowly adjusted downwards while ensuring good measurement conditions. Settings with good electron beam transmission were known down to about 400 eV.

To reach lower energies, one starts from these settings and reduces the cathode voltage until almost no TOF signal is visible on the oscilloscope. This leads to lower electron beam currents and also has a negative effect on transmission. To increase the transmission and current again, the potentials of the surrounding electrodes must be adjusted: Anode back, anode front, focus left and focus right. The drift tubes one and two also have some influence on the transmission. When the signal-to-noise ratio has been improved by the above adjustments, the cathode potential can be lowered further.

It is also possible to reduce the potential of drift tube four to achieve lower energies. This can be done in larger steps than lowering the cathode, as it does not affect the electron beam as much as changing the cathode potential. The electron beam is on its trajectory when exposed to the potential of DT4, and is only accelerated towards DT4, but is not otherwise affected in its movement. However, to reach very low energies, the cathode must also be lowered, as the potential of DT4 must eventually be close to zero.

When adjusting all the surrounding electrodes, one has to pay attention to the

transmission loss of the electron beam. In particular, the rear anode tends to absorb a substantial proportion of the current. Often this is up to 85% of the total current, especially at low energies and low currents. The power supplies that POLAR-X uses for its electrodes can handle up to 1 mA of current. It is important that the losses on an individual electrode are kept below this value to ensure that the power supplies can maintain their defined potential. If the current is increased above this value, the potential of the electrode may change and the beam may be diverted. In our experiment, we limited the maximum current loss to 0.6 mA per electrode to protect the power supplies and the electrodes from excessive currents.
When changing the potential of an electrode, it can sometimes happen that the electrode is struck by the electron beam and becomes charged in the process. This can alter the potential of the electrode so greatly that the beam is completely diverted towards a single electrode. If this occurs, the beam must be quickly switched off to prevent damage and allow the charge to be removed from the electrode so that the beam can be realigned.
At low energies, the cathode potential is low enough that the total current is less than 1 mA, so no matter how bad the transmission, the current will not be large enough to damage the equipment.
With a change in energy, the speed of the electrons in the electron beam changes, and so does the trajectory of the beam in the EBIT. This can lead to poorer transmission values. You can also adjust the gun position to change the trajectory of the electron beam. This changes where the electron trajectory begins and can greatly increase transmission.
The biggest change compared to high energies is in the Sikler lens potentials. All the voltages of the Sikler electrodes had to be increased by about 1 kV to get a more focused particle beam towards the extraction. It was also necessary to increase the injection pressure to enhance the intensity of the ion signals.
The process of finding good settings for low energies proved to be very tedious and difficult. A small change in a parameter can cause the signal to be lost, after which no further optimisation is possible. You have to be very careful which parameters to change and how much to change them to optimise the signal.
Below is a table of the optimised experimental parameters for low beam energies, which remain largely constant throughout the course of this experiment.
Some of these parameters may be changed slightly to optimize the signal strength. Parameters were not varied unless explicitly stated.

4.2 Spectra

The TOF spectra are taken from the oscilloscope. The oscilloscope is set up to communicate with the PC using Python. The spectra are stored as two arrays, one representing the time axis and the other the signal intensity.
To measure these spectra in a systematic way, we used a measurement scheme implemented in Python. This scheme was designed to vary the voltage of an electrode while keeping the other experimental parameters constant. In the program a start and stop point of the voltage is defined, as well as the step size. For each set of parameters, we take between ten and fifteen data sets from a selected range within the oscilloscope and average them to improve the signal-to-noise ratio. The selected parameter is then varied and the resulting spectrum is documented.
In addition to the spectrum, we also measure the pressure inside the injection. This allows us to correct for this parameter later if we find that it has changed significantly

Table 1: Experimental Parameters

Experimental Parameter	Value
Cathode	$-17V$
Focus Left+Right	$-80V$
Anode Rear	$1700V$
Anode Front	$1350V$
DT1	$2700V$
DT2	$820V$
DT4	$0 - 40V$
Extractor 1+2	$-1800 - 2000V$
Kick	$2500V$
Trap Depth	$8V$
Sikler Top, Bottom, Left, Right	$1000 - 1200V$
Bender Outer, Inner	$500 - 600V$
Breeding Time	$0.1s$
Trap Pressure	$1.7 \times 10^{-8} mbar$
Injection Pressure	$2 \times 10^{-5} mbar$
Transmission	$0.1 - 0.3$
Current	$0.5 - 1.3mA$

during the measurement. However, most of the measurements are short enough that the pressure does not change significantly. So we don't need to correct for it.

4.3 Measurements

Some of the results shown here display integrated data to better visualize the results of the measurements. The interpretation of this data will follow in the next section. We use a method of integration which will be discussed in section 6.1.
The first measurements made were attempts to ionize molecules and make them visible in a TOF measurement. An image of an early attempt is shown in Figure 9. The signal-to-noise ratio in this image is still very low.
We first injected methane and optimized the TOF signal. By identifying the individual peaks, we found good evidence that we were indeed able to produce and measure ionized dissociation fragments of methane. We decided to systematically find optimal parameters for the production and extraction of these dissociation products and then measure the spectra to study the behaviour of the individual fragments.
In Table 4.3 all measurements are listed with their corresponding ranges and step sizes.

Table 2: Overview of the measurements

Varied Parameter	Range	Step size
Trap depth	0 V-30 V	0.1 V
Trap pressure	1.3×10^{-8}mbar $- 2 \times 10^{-8}$mbar	0.05×10^{-8}mbar
Breeding time	0.001 s-0.13 s	0.0001 s
Energy Scan	23 eV-75 eV	0.1 eV
Disappearance Scan	16 eV-26 eV	0.1 eV

Figure 9: Picture of TOF spectrum displayed on the oscilloscope. Peaks from left to right: C^+, CH^+, CH_2^+, CH_3^+.

4.3.1 Trap depth

The trap depth is an important parameter to optimize for a good signal-to-noise ratio.
We injected methane and measured different spectra whilst varying the trap depth. One such measurement was made for a symmetric trap (see section 3.2) and one for an asymmetric trap.

Asymmetric trap

In the experimental setup section 3.2 we have described a symmetrical setup of drift tubes, where the potential of drift tubes three and five are equal. The difference between the potential of DT3 and DT4 gives the trap depth.
The first measurements we made were made using this symmetrical arrangement, whilst the later measurements used an asymmetrical trap. This means that the potential of DT3 is higher than that of DT5. We found that this greatly increased the signal intensity. This is due to the fact that when the kick voltage is applied, some of the ions are also accelerated towards the gun rather than the collector. Empirically, this seems to be about half of the ions, as the signal increases about two-fold when the symmetry of the trap is changed. This makes sense if the ion cloud is assumed to be centred in the middle of DT4. When the kick is applied, the large potential effectively divides the cloud in half and accelerates the two halves in opposite directions. This can be negated by an asymmetric trap, so that more ions are accelerated towards the extraction than towards the gun.
Unfortunately, we only started using this at the end of the experiment, so we did not have access to this superior method during the first experiments.
However, we did take the spectra of ethane without this asymmetric trap, which resulted in a worse signal-to-noise ratio in these spectra than would have been possible.

For ethane, we will focus on identifying the individual fragments of the dissociation, but we will not explore the behaviour of the spectrum as deeply as we did with the methane data. We will scan across a range of trap depths from 0 V to 30 Vin steps of 0.1 V.
The potential applied to DT3 was 60V while the voltage of DT5 was varied as described above. In figure 10 you can see the change in the ion populations of the methane spectrum as the trap depth is varied.
The power supplies we use for this experiment can deliver an electrical potential to within 0.1 V. There may be some inaccuracies in how the device determines a voltage, but these are less than 0.1 V, as can be easily seen by measuring the voltage of the power supply at low voltages with a voltmeter. This shows that the instrument is accurate in determining the potential in the range in which we use it, and we can assume that the reading of the trap depth is without significant error. This is also true for all other voltages measured by the power supplies, provided the voltages are read with the same accuracy. They are assumed to be free of error unless otherwise stated.

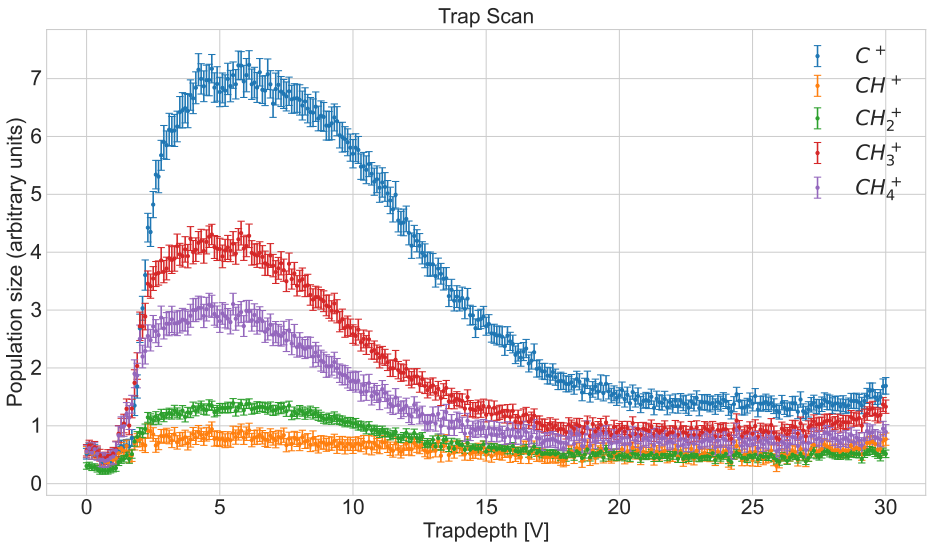

Figure 10: Population size of ions against trap depth. The errors are the standard error of the mean (calculated like discussed in section 6.1).

4.3.2 Pressure

The trap pressure has a significant impact on the population size. Particularly during extended measurements, the pressure may fluctuate and influence signal strength. In practice, our measurements are brief, and we can exert tight control over the pressure.
To investigate the correlation between ion population size and pressure, we varied the trap pressure from 1.3×10^{-8} mbar and 2×10^{-8} mbar in increments of 0.05×10^{-8} mbar by injecting methane.
The pressure gauge is not placed directly in the centre of the trap, as there is not enough space. Instead, it is located slightly below the trap centre and measures the gas pressure around the trap.
Increasing the trap pressure will increase the number of molecules in the trap centre. The dynamics of how large the different ion populations are and how they interact

with each other are partly determined by the number of particles present in the trap.
The pressure gauges we use in the experiment are accurate to about 10^{-11} mbar, the pressures we measure are many orders of magnitude above this value at about 10^{-5} mbar to 10^{-9} mbar. Due to the accuracy of the display, the error of the pressure reading can be assumed to be about 1% of the recorded value. However, this error is very small compared to the fluctuations in pressure that we encounter and can therefore be neglected.
There is some drift in the pressure over time as it takes time for the pressure inside the vacuum chamber to stabilise. This effect is particularly significant if the injection pressure has recently been changed, and the system has not had time to reach equilibrium. For this measurement, we are constantly changing the injection pressure. Therefore, after each adjustment, we have to wait for the pressure to reach a state of equilibrium.
However, there is still some inaccuracy in reading the exact value due to the fluctuation. To account for this, we observed the fluctuations in pressure. This showed that a reasonable assumption for this error is around 0.5×10^{-10} mbar. It is important to remember, as mentioned above, that the trap pressure is not the actual pressure at the center of the trap. Rather, it is the pressure of the gas surrounding the trap center. We do not claim to have an exact reading of the pressure inside the trap, only that the pressure inside the trap rises as the surrounding pressure rises.
When we recorded the spectrum for the pressure scan, the peak associated with CH_3^+ was missing. This is most likely due to a particular combination of extraction parameters causing the CH_3^+ ions not to be properly extracted.

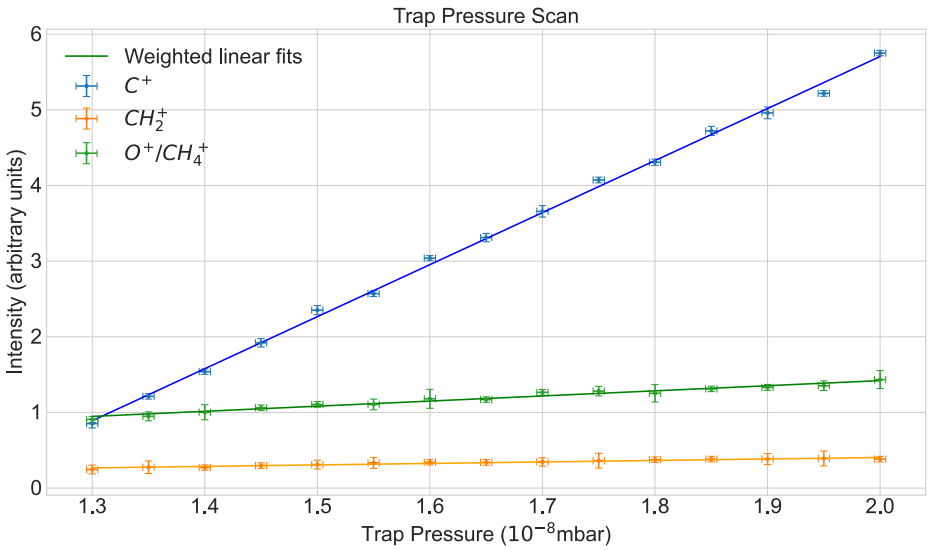

Figure 11: Population size of ions against trap pressure. Different colors indicate the ion populations that were inspected.

4.3.3 Current

The current of the electron beam is an influential parameter in maximising the signal strength. To understand how to optimally select the current, we varied the current while injecting ethane and took a spectrum at each step.

A systematic error was made in this measurement. Instead of simply varying the current while keeping the energy constant, the energy was also varied.
The current is increased by increasing the potential of the cathode. This also increases the energy, which can be compensated by decreasing the potential of the DT4 by the same amount as the cathode potential is increased. We failed to make this correction during the measurement.
Unfortunately, once we realised this error, we did not have the experiment available to repeat the measurement.
It would still be interesting. However, it is not too important for the continuation of the experiment. The current we can achieve is very limited due to the low transmission associated with low energies.
With a low current, it is best to get as high a current as possible to maximise the signal.

4.3.4 Breeding time

The breeding time is the time that the electron beam interacts with the cloud of molecules until we apply the kick voltage to extract the ions.
How long the electron beam interacts with the particles determines how many ions are found in the trap. It also affects how the ionization states are populated relative to each other, as this time also determines how long the different ion populations can interact with each other.
We varied the breeding time between $0.001s$ and $0.13s$ with a step size of $0.0001s$ and took a spectrum at each step.

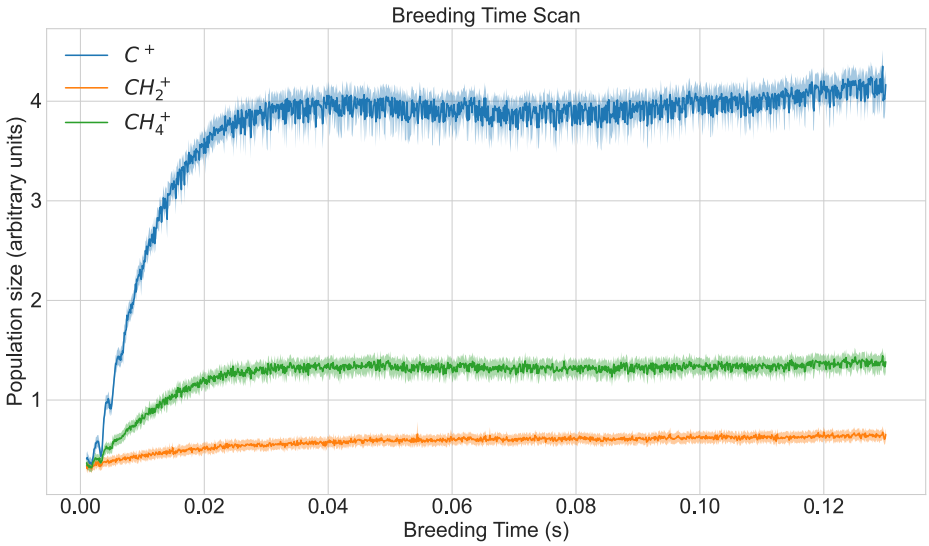

Figure 12: Population size of ions vs. breeding time. The bands around the plots indicate the standard error of the mean.

To obtain a periodic measurement scheme as described above, we used a Keysight 333500B series function generator. The electronic signal from this function generator can be visualised by connecting its output to an oscilloscope. We can see that we can easily generate a signal of the length and step size described above by measuring the resulting signal on the oscilloscope. For this reason, we don't assume any propagation time error in this measurement. We also don't assume any error

for other time parameters of similar length and step size generated by a function generator of the same type.
In Figure 12 you can see how the peak intensities change with the breeding time for methane.

4.3.5 Energy

Now that we have made all the measurements to determine how best to choose the experimental parameters to optimise the TOF signal, we will make measurements of the spectra of methane and ethane whilst varying the beam energy. As mentioned above, a symmetric trap was used for the ethane measurements, whilst an asymmetric trap was used for the methane measurements.
We chose an asymmetric trap for the methane measurement. One can see that the signal to noise of the ethane using a symmetrical trap is very similar to the signal to noise ratio of methane using an asymmetrical trap (see figures 17 and 21). For the ethane measurement, we increased the voltage applied to the channeltron for the short duration of the measurement. This caused more secondary electrons to be emitted in the channeltron, increasing the signal intensity. This was not done to the same extent for the methane measurement.
Care must be taken here as high voltages over long periods can damage the channeltron or cause it to overheat. Overheating causes the signal to degrade over time. For this reason we did not use this method of increasing the signal intensity for most of the measurements.

Disappearance of the spectrum

During the measurements we found that the signal is very reliably lost at beam energies of around 15 eV. We are studying this more carefully to better understand what limits our ability to go further down in energy.
To study this effect, we measure the spectrum of methane and lower the beam energy further down until the signal disappears completely.
It is important to think carefully about how the experimental parameters change during the measurement. The drift tube 4 is at zero potential during this measurement, as we are already close to the limit of how far we can reduce the beam energy. This means that to get to lower beam energies we have to lower the cathode potential. We have done this in steps of 0.1 V. This also lowers the current, resulting in a poorer signal. This limits how low we can set the energy and still measure a signal.

5 Modeling of the ion populations

In order to interpret the data in a meaningful way it is useful to create a model of the processes that influence how large a given ion population is. There are processes that add to a given ion population and processes that take away from it.
The rate of change of a given population n_i is given by [18]:

$$\frac{dn_i}{dt} = \frac{e}{j}(\sum_l n_l\sigma_l - n_i\sum_k \sigma_k) \tag{30}$$

The first sum is composed of all the processes that add to the population n_i the second sum consists of all the processes that remove ions from the population n_i, where e is the elementary charge and j is the current density of the electron beam:

$$j = \frac{I_{collector}}{\pi r_H^2} \tag{31}$$

with r_H being the Hermann radius, as defined in section 3.4.1.
One can formulate such a differential equation for every ion population present in the trap. As many processes take away from one ion population and add to another these differential equations are coupled. This set of coupled differential equations is solved numerically by the Runge-Kutta method.
This method can be used to solve an initial value problem of the form[27]:

$$\frac{dy}{dt} = f(t, y), y(t_0) = y_0 \tag{32}$$

where y is an unknown function we would like to solve for. The rate of change over time of this function is given by the function $f(t, y)$ and its initial value at time t_0 is y_0. One defines a step size h which will dictate the steps between iterations. This can be used to define the iterative solution to this problem:

$$y_{n+1} = y_n + \frac{h}{6}(k_1 + 2k_2 + 2k_3 + k_4) \tag{33}$$

and

$$t_{n+1} = t_n + h \tag{34}$$

where the k_i are defined as:

$$k_1 = f(t_n, y_n) \tag{35}$$

$$k_2 = f(t_n + \frac{h}{2}, y_n + h\frac{k_1}{2}) \tag{36}$$

$$k_3 = f(t_n + \frac{h}{2}, y_n + h\frac{k_2}{2}) \tag{37}$$

$$k_4 = f(t_n + h, y_n + hk_3) \tag{38}$$

where y_{n+1} is the approximation of $y(t_{n+1})$ provided by this method. The next solution is determined by the weighted average of four increments located inside the step size. We will not describe this method further here. Rather we will discuss what reactions we will consider to formulate the differential equations.

Included processes

There are many processes that can occur in the EBIT. We will primarily focus on reactions that have a larger cross-section than $1 \times 10^{-17}\,\mathrm{cm}^2$.
Neutral particles are not trapped in the EBIT and thus are mostly lost from the system. These reactions remove ions from a population without adding to another. It follows that we will only consider the electron impact ionization of neutral methane but not its neutral fragments. Neutral dissociation and dissociative recombination will not be considered as their cross-sections are low. We will consider the processes of dissociative excitation and ionization.
For atomic ions, we will consider direct ionization from a given charge state to a larger one. As we only include carbon ions in our model, we use [32] for their ionization cross-sections.
There are many more processes that one may include if one were looking for a complete prediction of the behavior of the ions in the EBIT, such as dielectronic recombination. We will not do so here, as one will see that much of the data can be interpreted without the inclusion of said effects. All of the reactions in the molecules that are considered can be seen in the appendix.
In figure 13 we show schemes of the processes we consider. All processes that are displayed in these schematics are included in the differential equations.

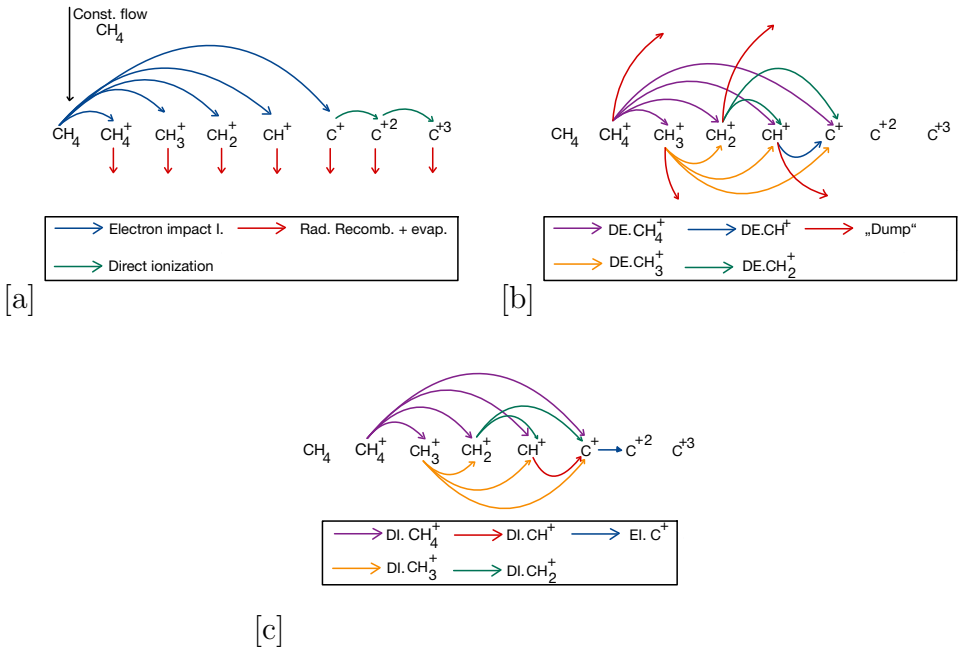

Figure 13: Three Schematics show all processes considered in the model. Arrows indicate from which population ions are removed and to which population they are added. (a): electron impact ionization of neutral methane, direct ionization of carbon ions. Red arrows indicate the losses from radiative recombination and evaporative losses. (b): dissociative excitation. Red arrows: labeled "Dump", consider all processes that result in neutral fragments, which are lost in the model. (c): dissociative ionization from above 28 eV energy. All above processes are considered simultaneously but are not shown in one single schematic to ensure visibility.

For losses of ions we also consider radiative recombination and evaporative cooling. Because of the temperature distribution there will be ions that have enough thermal

energy to escape from the trap. The rate at which ions escape because of this effect can be described by [28]:

$$\frac{dn_i}{dt} = -n_i \nu_i \left[\frac{e^{\omega_i}}{\omega_i} - \sqrt{\omega_i}(\mathrm{erf}(\omega_i) - 1) \right] \tag{39}$$

with

$$\omega_i = \frac{q_i V_w}{k_B T_i} \tag{40}$$

where ν_i is the coulomb collision rate, V_w is the trap depth and T_i the ions temperature. ν_i is calculated by[29]:

$$\nu_i = \frac{1}{3\pi^{1/2}} \frac{n_i}{V_{ion}} (\frac{q_1 q_2}{4\pi\epsilon_0})^2 \frac{4\pi}{m_i^{1/2} T_i^{3/2}} \ln(\Lambda) \tag{41}$$

where m_i is the ion's mass, q_1, q_2 are the charge states of the ions, V_{ion} is the volume of the ion cloud and $\ln(\Lambda)$ is the coulomb logarithm.
The ion temperature can be approximated by[19]:

$$T_i \approx \frac{q_i V_w}{5 k_B} \tag{42}$$

and $\ln(\Lambda)$ can be assumed to be around 15 for laboratory plasmas[29]. The volume of the ion cloud will be assumed to be of cylindrical shape with a length of 1mm and a radius of 5 times the Hermann radius of the electron beam [30].
In addition to the losses due to evaporation, we will also consider radiative recombination (see section 2.1.2). The loss of ions due to radiative recombination and evaporation will be considered for all ions. There might be deviations from the cross sections for the molecules compared to the atomic ions for these expressions but they will be assumed to be small.
As an example of a differential equation we show CH_4^+'s population:

$$\frac{dn_{CH_4^+}}{dt} = \frac{e}{j} \left[n_{CH_4} \sigma_{CH_4 \to CH_4^+} - \left(n_{CH_4^+} \sum_{DE.+DI.} \sigma_{CH_4^+ \to CH_x^+} + \frac{dn_{CH_4^+,\text{EV., R.R.}}}{dt} \right) \right] \tag{43}$$

The first term considers the electron impact ionization of neutral methane to CH_4^+, the sum considers all reactions of dissociative excitation(DE.) and ionization(DI.). In the case of CH_4^+ these only decrease the population. The last term is the combined rate of losses form evaporation(EV.) and radiative recombination(R.R.)
We will not show all differential equations. They can be reconstructed from our description of the considered processes, the schemes, and the tables in the appendix. The stream of neutral methane is modeled by keeping the population of CH_4 constantly at 1. This allows for replenishment of the ions which would otherwise dissociate into carbon.

The cross sections used for this model are not without error [5]. This leads to error propagation in the numerical solution. In this work, we will not discuss the error further due to the time constraint of this thesis.

In Figure 14 we show the solution of the coupled differential equations. We assume all ion populations to be zero at time t=0 and use 40000 steps with a step size of 0.00001 at an energy of 34 eV:

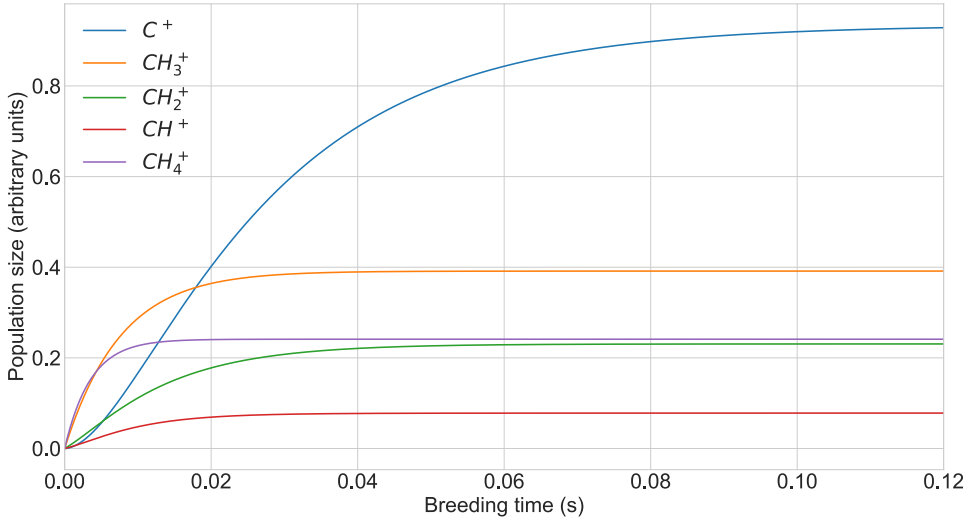

Figure 14: Model of ion populations vs. time. Each population converges to a constant value.

The molecular ion populations each converge after around 0.02s or slightly before that. The population of C^+ converges later. If we also include C^{+2} and C^{+3} we have to go up in beam energy to around 60 eV which can be seen in figure 15.
In this figure, we only show the carbon populations, as the molecular ions all converge for every energy between 20 eV and 70 eV. However, the carbon populations behave differently here. The C^{+2} population only converges after around 0.35s, while the C^{+3} population does not converge at all. This is because of the reactions we consider in the model. The energy is not large enough to ionize C^{+3} so the only effects that we consider that remove ions from this population are the evaporation and the radiative recombination. The sum of these effects is small compared to the cross section of the ionization of C^{+2} so the population of C^{+3} needs to be very large for these effects to counteract the ionization of C^{+2}.

We now calculate a solution for the ion populations for every energy between 20 eV and 70 eV with a step size of 0.1 eV and take the value of the populations at 0.25 s breeding time. This is the value we often use for breeding time. The populations of C^{+2} and C^{+3} do not converge around this time. During the time of constructing this model, the EBIT was unavailable, so we were not able to carry out measurements of these populations as a function of breeding time. We will use the value at these times as we can neither confirm nor deny this divergent behavior in the real experiment.
This allows us to plot the population as a function of the beam energy (see Figure 16)
We will discuss how the model compares to the data in the next section.

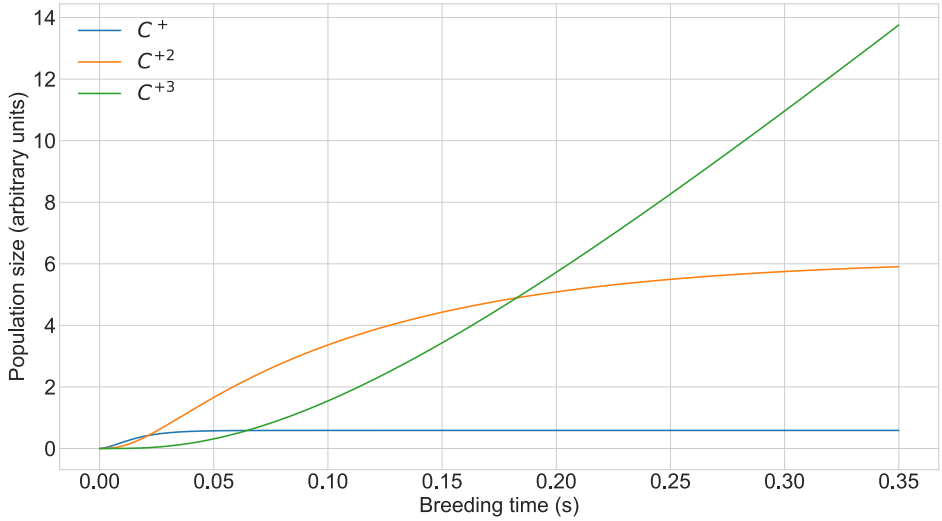

Figure 15: Model of carbon populations vs. breeding time. The populations of C^{+2} and C^{+} converge, while C^{+3} diverges.

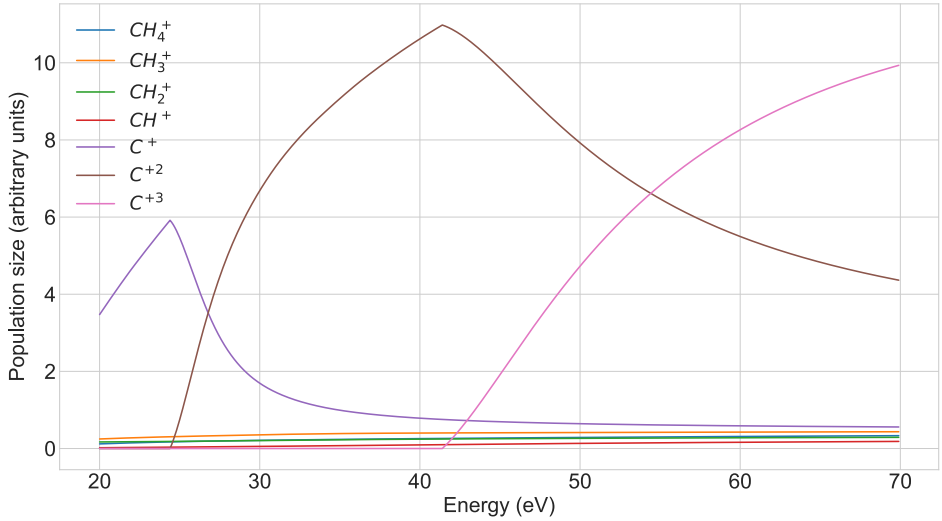

Figure 16: Model of the ion populations as a function of electron energy.

6 Data analysis

In this part of the thesis, we analyze the data taken in Section 4. We will discuss how we integrate the spectra and how we correct for systematic errors in the spectra. Different interpretations of the data and the following implications are discussed.

6.1 Integration

One of the most important aspects of interpreting the data is having a good measure of the different ion populations. Like we saw in Section 3.9, the peaks in the TOF spectrum correspond to the different ions traversing the beam line at different velocities. We use the integral of these peaks as a measure of how many ions of a certain kind are present in the trap. One of course has to consider the limits of this assumption, like we did in Section 3.8, but like we discussed, this is a reasonably accurate measure of the ion population.
To get a measure of the intensity of the individual peaks, we define a region of interest (roi) around a peak and use the composite-trapezoidal rule to numerically integrate the peak over this region. The region we chose does not include the ringdown. Like we saw in Section 3.9, the ringdown corresponds to the discharge of a capacitor. All the charge that was deposited from the charge pulse must discharge again. Thus, the integral of the ringdown is the same as the integral of the peak. Because of this, we chose not to include it in the measure for the ion population.
In the composite-trapezoidal rule, multiple trapezoids are used to approximate the integral of a curve[11].
The simplest form of this is to use a single trapezoid to approximate the integral of a function over the interval $[a, b]$:

$$\int_a^b f(x)dx \approx (b-a)\frac{1}{2}(f(a)+f(b)) \tag{44}$$

Of course, this is a very rough approximation of the true value of the integral. One may improve the approximation by including a larger number N of trapezoids and consequently summing all the respective areas:

$$\int_a^b f(x)dx \approx \sum_{k=1}^{N} \frac{f(x_{k-1})+f(x_k)}{2}\Delta x_k \tag{45}$$

where Δx_k is the width of a single trapezoid. When integrating over a set of discrete data points that have uniform spacing, like we find in our data, Δx_k corresponds to the spacing between two data points in the x-direction (time in our data).
The error E of this numerical integration can be estimated to be [11]:

$$|E| \leq -\frac{(b-a)^3}{12N^2} max|f''(x)| \tag{46}$$

where $max|f''(x)|$ is the maximal value of the second derivative of the data in the interval $[a, b]$. We will not prove this here. For the full derivation, one may look at [11].
In practice, we will determine the second derivative of the data using the gradient:

$$f'(x) \approx \frac{f(x+\Delta x)-f(x)}{\Delta x} \tag{47}$$

with Δx being the distance between two data points. We will use this function again on the computed gradient to get the second derivative of the array, from which we can take the maximal value.
The distance Δx between two data points in the spectra is very small and is determined by the time resolution of the oscilloscope. Because of the high resolution of the oscilloscope, we will neglect the error of the second derivative, which comes from the data points being discrete rather than a continuous function.
Because of the high resolution of the oscilloscope, the employed method will provide a very good approximation of the integral of the individual peaks. The error of the numerical integration will be very small. It is often about three to four orders of magnitude smaller than the value of the integration. We will ignore this error.
Rather, we will consider the statistical error that one gets when using the mean of many spectra to produce the spectrum we will use for the integration. To quantify this error, we will numerically integrate every peak of a spectrum and calculate the standard deviation of the mean. The error of an individual measurement will be assumed to be the standard error of the mean:

$$\mathrm{SE} = \frac{\sigma}{\sqrt{n}} \tag{48}$$

where SE is the standard error, σ is the standard deviation, and n is the number of spectra that were used for the mean.
One also has to consider that the baseline of the spectra is not at zero but rather slightly above it. Before we can use the numerical integration, we have to correct this by lowering the spectra in such a way that its baseline is zero. One finds this baseline at low TOF values as there are few peaks and the signal is only composed of the baseline.
Also, for most of the measurements, we will not correct for the ringdown. The ringdown will influence the intensity of certain peaks, but the influence is small enough for us to ignore it for most measurements. Later on, when we discuss the energy scan, we want to get as good a representation of the ion populations as we can get. Then we will correct for the ringdown.

6.2 Peak identification

Before we talk about the measurements that concern themselves with finding optimal experimental parameters, we will identify the different peaks in the spectrum of methane and ethane. This will be helpful later on, as we will often analyze how an individual peak behaves when varying a certain parameter. To make it clear what peak we are talking about, we will first identify all of the peaks and lay out the evidence for their identification. We give the q/m ratios in units of $\frac{e}{u}$, where e is the elementary charge and u is the atomic unit.
There is an important impurity in the trap that we have to consider in the analysis of the data. The trap always contains some water molecules. These stem from water vapor from the outside that is difficult to remove from the vacuum system. Some of this water vapor dissociates into hydrogen and oxygen upon interaction with the electron beam at small energies. In the measurements, we will find varying amounts of water vapor in the trap. The H_2O^+ and the OH^+ peaks are easy to identify and cause no problem in the measurements as they don't influence other peaks. The same is true for the products of dissociation, which often include O^{2+}, O^{3+} and H^+. However, the O^+ peak causes some ambiguity in the TOF spectra. The q/m of O^+ is 1/16; this is the same q/m value as CH_4^+. The peak that is associated with a q/m

of 1/16 is composed of the contributions of the ions O^+ and CH_4^+. If there is a lot of water present, it is hard to say how large an impact the O^+ has on the integral of the 1/16 peak. The influence of this will be discussed in detail for each spectrum, as it is different for each measurement.

6.2.1 Methane

In figure 17, we show the spectrum of methane at an energy of 57 eV, including an identification for each line. We will now lay out the evidence for this identification. In the later section 6.6, we will further talk about the height of the individual peaks and how they change with energy. For now, we just want to identify the peaks.
When this spectrum was taken, we injected methane at a trap pressure of around 2.4×10^{-8} mbar. We expect methane and all of the dissociation products to be present in the trap. Further, we can expect to ionize carbon up to +3 as we are at 57 eV beam energy, which is well above the ionization level of C^{2+} of 47.9 eV [12]. Similarly, we expect to see ions of oxygen up to +3, which will be ionized at 54.9 eV[12]. We also expect some water and its dissociants to be present.
In conclusion, we expect the following peaks in the methane spectrum:

$$C^{+3}, C^{+2}, C^+, CH^+, CH_2^+, CH_3^+, CH_4^+, H_2O^+, OH^+, H^+, O^+, O^{2+}, O^{3+}$$

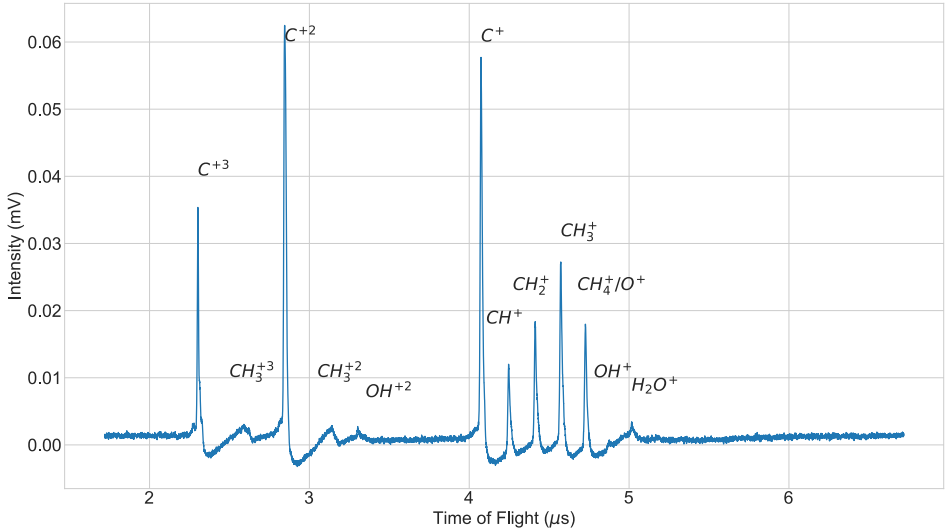

Figure 17: TOF spectrum of methane with identification of the ions associated with the peaks. The higher the TOF value, the smaller the q/m ratio of the ion.

The most important tool to determine the q/m values of the peaks is the so-called TOF calibration. For this, one guesses the q/m ratios of some peaks and then verifies the guess by fitting the function for the time of flight to the q/m values:

$$t = \frac{\Delta x}{v} = \frac{\Delta x}{\sqrt{2U_{\text{kick}}}} \frac{1}{\sqrt{(\frac{q}{m})}} \tag{49}$$

To identify the peak, we define a threshold in height, above which we consider the signal to be a peak. The maximum of the signal will then be used to determine the position in time. As most of the peaks are close to symmetrical, this is a good

approximation. We assume an error for the position of the peak in time when using the position for the q/m calibration. As the peaks are gaussian in form, we take the full width half maximum as the error of the time position.

For the first guess, we can use our expectation of the ions we will find in the trap. We know that methane has four products of dissociation that are all very close in mass.
CH_4^+ has a q/m ratio of 1/16, CH_3^+ has a ratio of 1/15, CH_2^+ has a ratio of 1/14, CH^+ is 1/13, and finally C^+ has a ratio of 1/12. We use this guess for the structure located between 4.1 μs and 4.7 μs. The resulting fit is shown in figure 6.2.1.

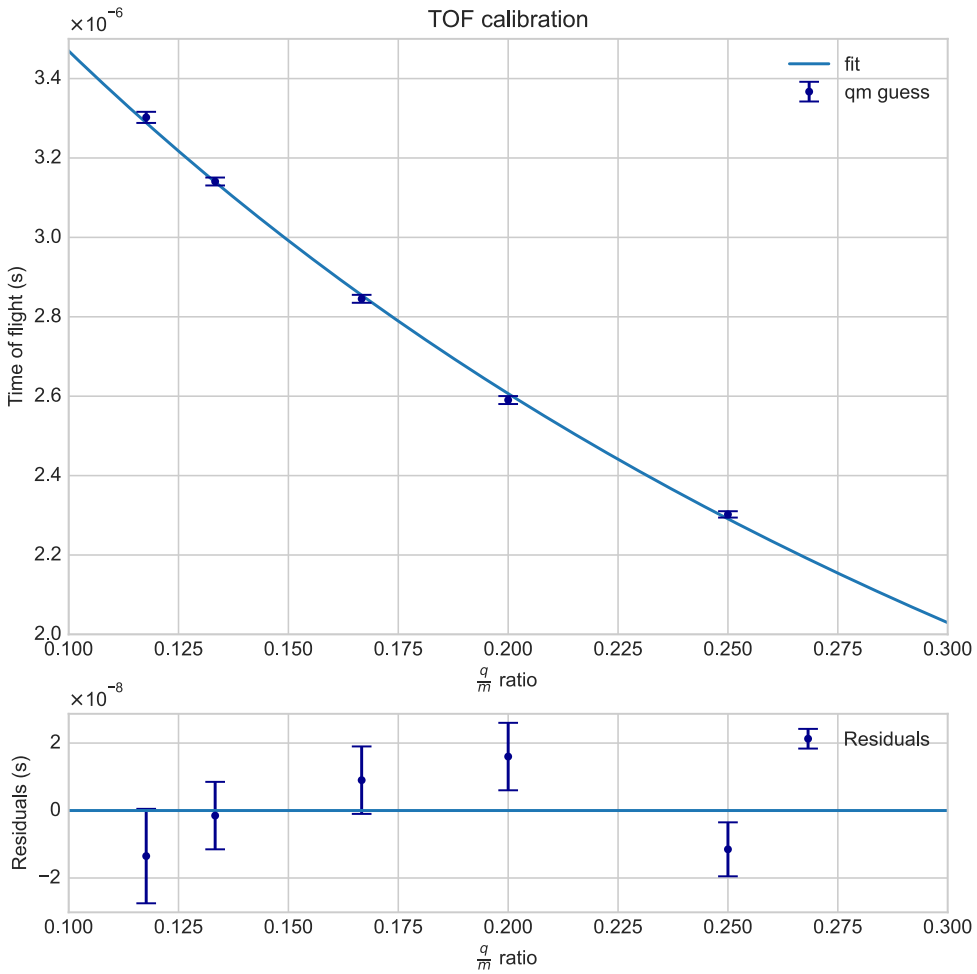

Figure 18: TOF calibration methane. Fit created using weighted linear regression. The errors in time are full-width-half-maximum of the peaks.

The fit works very well for this guess.Now that we have established the first five peaks, we are able to identify the rest of the peaks more easily, as we can just look at the expected q/m values and compare them to the spectrum.
We know that we will always find varying amounts of water in the trap. The q/m values for H_2O^+ are 1/18 and for OH^+ 1/17. These correspond to the small peaks at roughly 4.8 μs and 5 μs.

Some of the structures of the spectrum first arise at higher energies. This is why we choose to show the spectrum at 57 eV, to have a spectrum where all the structures are present. Like we stated above, we expect C^{+3} and C^{+2} to be present at this energy as they are ionized at around 24 eV and 48 eV [12]. If we take a look at the spectra around this energy, we find that there are two respective peaks that arise. One of them arises at roughly 2.8 μs at around 24 eV and the other at 2.4 μs at an energy of 45 eV.
There is more evidence to support this claim. The peak is of great intensity. This large intensity is only reached by atomic ions. The reason for this is that the amount of molecular ions is more strongly limited by dissociation, while atomic ions don't break up into other parts. This implies that this peak is an atomic ion. The only other atoms present in the trap that are of sufficient concentration to lead to a significant signal of this kind are hydrogen and oxygen. H^+ has a q/m ratio of 1 and is the earliest peak we find in the spectrum. The only other option is oxygen. The ions O^{2+} and O^{3+} are ionized at an energy of 35.1 eV and 54.9 eV. If we inspect the spectrum around these energies, we find no peaks.
No less is true for the peak we are trying to identify. 43.8 eV is too large an energy for O^{2+}. It is also significantly too small to ionize O^{+2} to get O^{3+}. The only remaining option is that this peak corresponds to C^{+3}.
Like we mentioned above, we don't find any peaks emerging at the ionization energy of oxygen. Also, if one looks at the peaks of H_2O^+ and OH^+, one finds that they are of small intensity compared to the peaks of the dissociation products of methane. From this, we draw the conclusion that in this measurement, very little water is present in the trap, thus no significant amount of oxygen ions are produced.
This is very advantageous for later interpretations of the methane spectrum. As water leads to ambiguities in the peak of CH_4^+ . We can ignore the influence of O^+ on this peak.
To identify the remaining three peaks at around 2.5 μs, 3.1 μs, and 3.2 μs, we consider possible q/m ratios, given the peaks we have already identified and think about possible molecules that could have these values. A TOF calibration will not be done here, as the peaks have bad signal and are very broad. This leads to large uncertainties.
Before doing the identification, one might guess that the peaks at 2.5 μs and 3.1 μs might be reflections of the large carbon ion peaks, as we briefly mentioned in Section 3.9. This is not the case. If one looks at the intensity of these smaller peaks, one finds no correlation between the larger carbon peaks and the smaller peaks.
We already identified the peak of C^{+3} and C^{+2} which have q/m ratios of 3/12 and 2/12 so the peak between them has to have a q/m that lies between these values and the two peaks to the right of C^{+2} have to have a slightly smaller q/m than 2/12. For the peak at 2.5 μs we a q/m of 3/15 is fitting as it lies between 3/12 and 2/12. This would corresponds to CH_3^{+3}. As we find CH_3^+ in the trap it is in principle possible to ionize further to get to this state of ionization. Similarly, we guess a q/m ratio of 2/15 for the peak at 3.1μs as it is slightly smaller than 2/12 and would correspond to CH_3^{+2} which like we said can in principle exist in the trap.
The last peak at 3.2 μs is 2/17 which is slightly smaller than 2/15 and would correspond to OH^{+2}. Again we are able to produce this ion in principle since we find OH^+ in the trap.
In this spectrum we didn't record the hydrogen peak. This peak will be seen in other spectra. However, we decided to zoom in further into the spectrum and ignore this peak to get better resolution of the other peaks that are of more interest to us.

The hydrogen peak has the issue of being very far away from the peak we optimized the spectrum for. As a consequence its extraction efficiency is rather bad compared to other peaks and change in peak height is not really representative of the true amount of hydrogen in the trap.

6.2.2 Ethane

Now we will identify the peaks in the spectrum we took for ethane. Here we will use many of the arguments we used for the peak identification of methane; thus, we will only highlight some of this process. The spectrum we show below was taken at an electron beam energy of 34 eV.
Here, it is useful to again think about the ions we expect to find in the trap. When we inject ethane (C_2H_6) at a pressure of around 2.4×10^{-8} mbar, we expect to find the dissociation products of it where only single hydrogen atoms have broken away. We also expect some water and its dissociants to be present in the trap. It is also possible that C_2H_6 will dissociate to CH_4, which is methane. If this happens, we will find the dissociation products of methane again, like we did in the methane spectrum. This also includes ions of carbon.
In conclusion, we expect the following ions to be present in the signal:

$$H^+, C^{+3}, C^{+2}, C^+, CH^+, CH_2^+, CH_3^+, CH_4^+, H_2O^+, OH^+, H^+, O^+,$$

$$O^{+2}, O^{+3}, C_2H^+, C_2H_2^+, C_2H_3^+, C_2H_4^+, C_2H_5^+, C_2H_6^+$$

The first peak is easy to identify. It is located slightly above 1 μs. This peak is the peak associated with H^+ which has the highest q/m value in the trap of 1.
It is also clearly visible that we see a structure composed of seven peaks between 4 μs and 5 μs. This is roughly at the same position where we found the dissociation products of methane, which we expected to be present in this spectrum, as we mentioned above. We do a TOF calibration where we guess the peaks to have q/m values of 1/12, 1/13, 1/14, 2/29, 1/15, 1/16, and 1/17.
The double ionization of ethane's fragments leads to some ambiguity. The peak for the q/m value of 1/13 could also belong to $C_2H_2^{+2}$ as the q/m ratio of this ion is 2/26=1/13. The same ambiguity is possible for the other methane dissociation peaks.
It is interesting to note here that the peaks that may show some ambiguity have a greater intensity than the peaks that are only associated with one ion species. This makes sense when you consider that two components are adding to the same peak rather than one ion.
This ambiguity is also why we won't take a closer look at the development of each individual peak, as it is difficult to separate these ambiguous peaks into their individual components.
In figure 6.2.2 we show the resulting TOF calibration and the associated fit.
The fit works well. However, we have more evidence for the identification we provided than just the TOF calibration.
We don't find any ionized water but only OH^+. The experimental parameters may cause the water ions to be lost during production or extraction. Again, we cannot observe any ions of oxygen, which implies that the trap holds very little water.
In the same way we did above, we can identify the carbon peaks by observing their appearance at the given ionization energies. Here, the energy of the beam is large enough to produce carbon ions up to C^{+2}. Very close to the peak of C^{+2}, one can

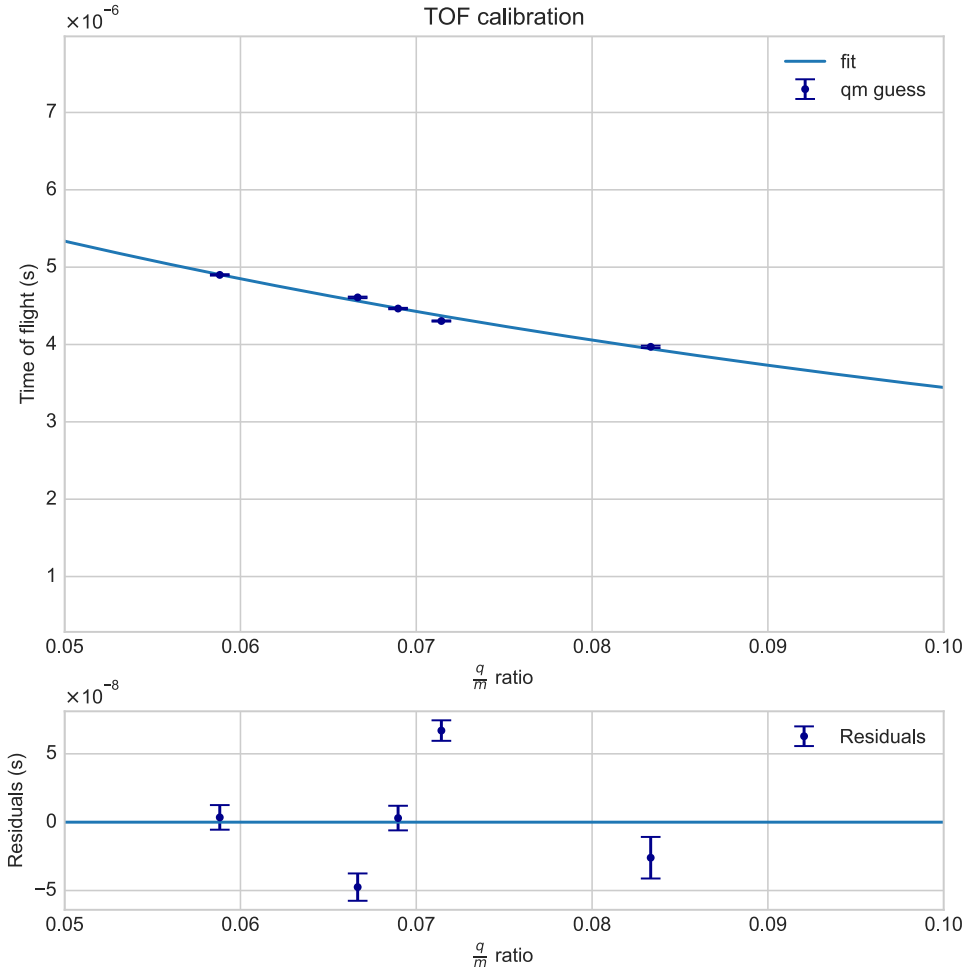

Figure 19: Residuals of the middle of the ethane spectrum. Fit created using weighted linear regression. The error in time is the full-width-half-maximum of the peaks.

see a small rise in intensity in the ringdown. This is very close to the peak and is thus unlikely to be the peak of another ion, as there are no possible q/m values that would be this close to this carbon peak. Also, the peak intensity is very large, thus making electronic artifacts like reflections more likely. This rise in intensity is most likely just a reflection of the carbon peak and is thus not to be interpreted as a real signal from ions.
The same goes for the small structure that can be seen next to the C^+ peak. As the peak is very large, it is reasonable to assume that this structure is a reflection of the carbon signal.
The structure between 5.7 μs and 6.3 μs is very small. As it is located at larger TOF values, it has to be composed of ions with a large q/m ratio. One can easily count the peaks as six in total. These peaks suggest themselves to be the dissociation products of ethane that have two carbon atoms, as there are exactly six of them. There is: $C_2H^+, C_2H_2^+, C_2H_3^+, C_2H_4^+, C_2H_5^+, C_2H_6^+$ which q/m ratios are. We can again look at a TOF calibration in figure 6.2.2 to prove this guess.

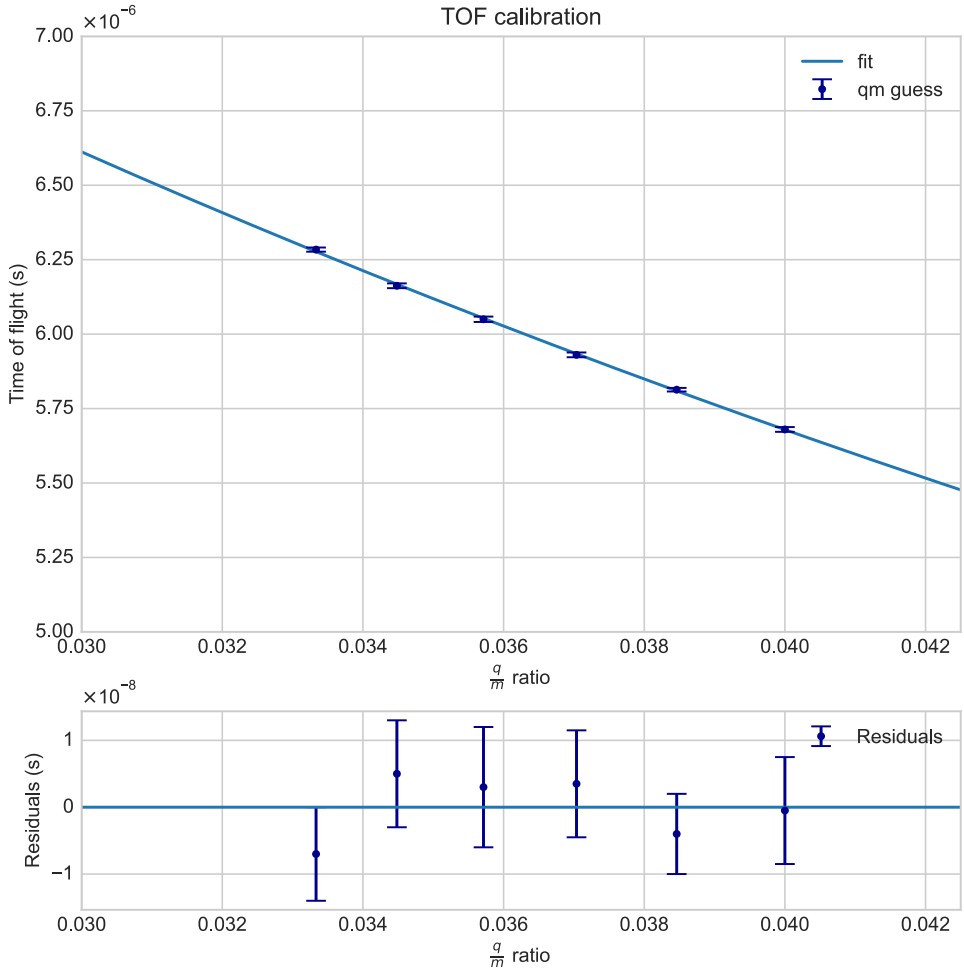

Figure 20: TOF calibration of the right side of the ethane spectrum. Fit created using weighted linear regression. Error bars are full-width-half-maximum of the peaks. The error bars are large for these data points as the peaks are very small and as a consequence very wide.

The errors are large as the peaks are small and wide in form. If we consider teh fit and our initial expectations of the ion composition, we can confidently identify the peaks.
We also find a very small peak somewhat close to the hydrogen peak at 1.5 μs. This peak probably belongs to H_2^+ with a q/m value of 1/2. Light elements like carbon and oxygen that we find in our trap almost all have a q/m ratio of 1/2 when they are stripped of all of their electrons. However, the energies that we are using the EBIT at are far too low to fully strip these elements bare, so this peak cannot be associated with them.
The fact that the peaks are of small intensity makes sense, as we are not optimizing for neither their production nor their extraction. They are far away in q/m values from the center of the dissociation products of methane that we have optimized for here. Also, the extraction of these heavy ions would benefit from other extraction parameters of the Sikler lens, bender, and kick voltage to be more specialized to

their mass.
One can find what might appear to be small peaks in between the true peaks. One may look, for instance, in between the peaks we associated with $CH_3^+/C_2H_6^{+2}$ and CH_4^+.
This is likely to be random noise in the signal, as there are no obvious q/m ratio candidates for these TOF values. To be sure, one may take a spectrum with again improved settings and also an asymmetric trap to increase the signal-to-noise ratio. Here, we won't identify these structures, as we have no reason to believe that they are associated with any real q/m values.
However, this is fine for our purposes, as we only show this spectrum to provide an example of what kind of ions we are able to produce with the EBIT at low energies and are not necessarily interested in studying their behavior. Although this may be very interesting for future studies.

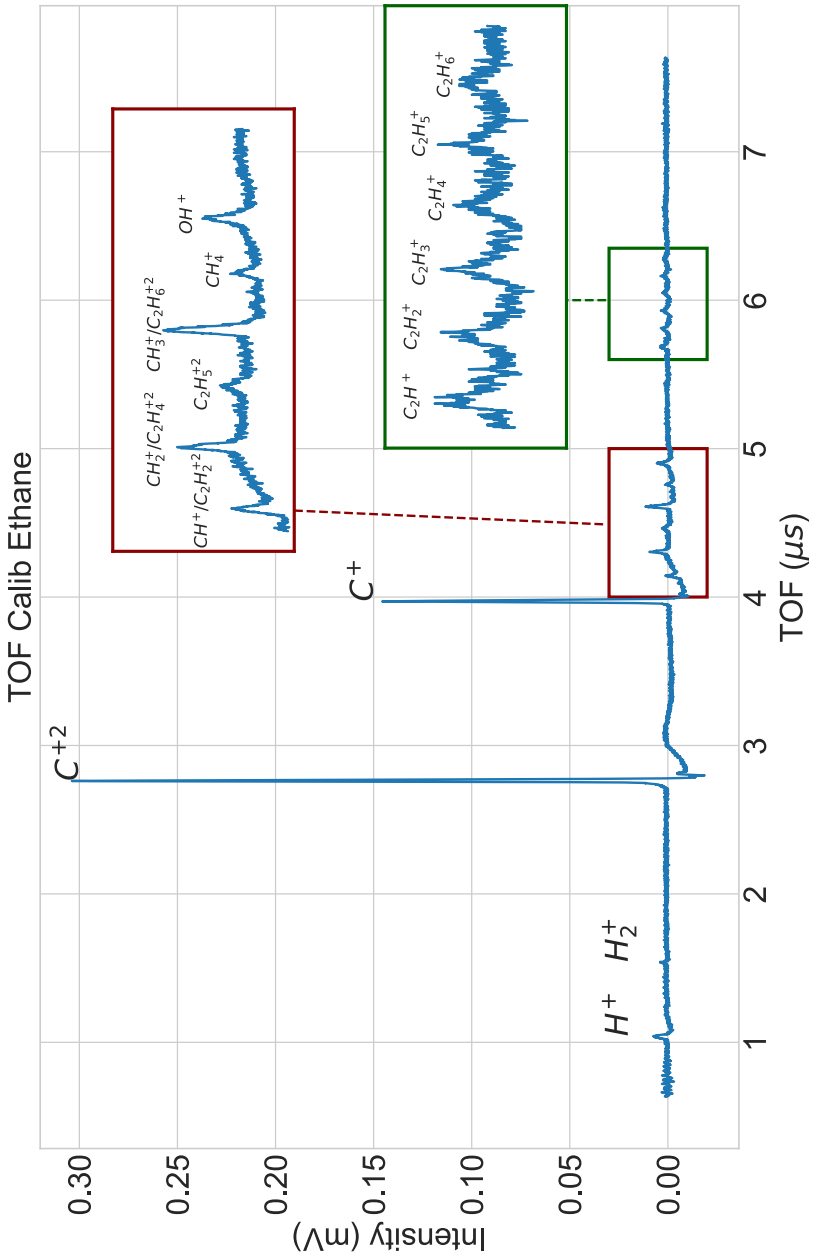

Figure 21: TOF spectrum of methane with line identification. The colored boxes are zoomed-in sections from the spectrum. The singly charged methane and doubly charged ethane fragments are highlighted in the red box. The singly charged fragments of ethane are highlighted in the green box.

6.3 Pressure

We varied the pressure inside the trap and took a spectrum at each step, like we described in Section 4.3.2. This measurement was done using a symmetric trap.
There is no CH_3^+ peak, which, like we already mentioned, is most likely because the experimental parameters we chose were of such a nature that the production and extraction of CH_3^+ were greatly suppressed. One can also notice that the peak that corresponds to CH_4^+ and O^+ is very large compared to the other peaks, except for the peak of C^+. This implies that there is a lot of oxygen and, consequently, water in the trap. However, we will later show that this is not an issue as the water content stays constant during the experiment while the methane content changes. Thus, the influence of O^+ does not play a role in how the peak changes.
In Figure 22, one can see the spectrum and the regions of interest we determined for the integration of the peaks. We chose not to correct for the ringdown in this measurement, as all the peaks we are considering are not significantly located within the ringdown of another peak.

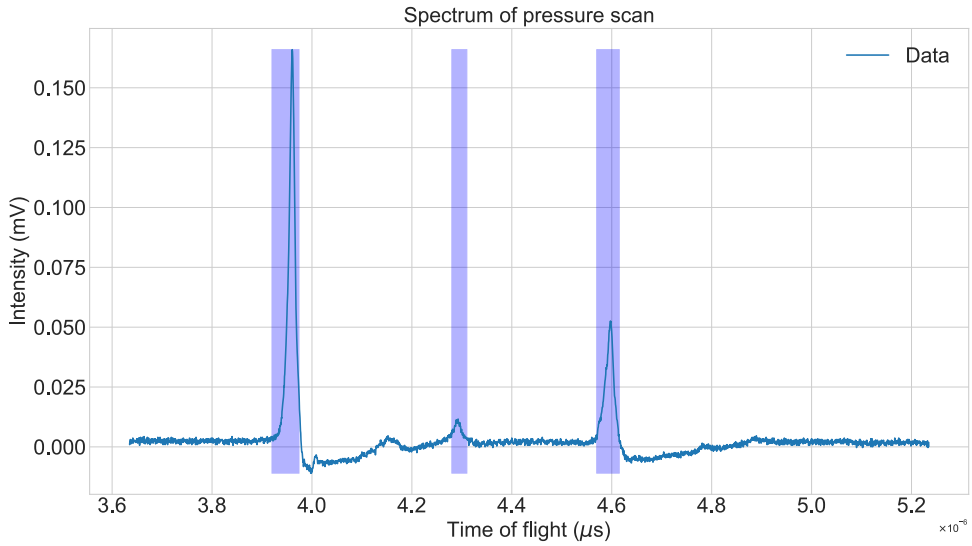

Figure 22: Spectrum of the pressure scan. Blue bars indicate the interval of the integration. Left peak: C^+, middle: CH_2^+, right: O^+/CH_4^+.

We only focus on the O^+/CH_4^+, CH_2^+, and the C^+ peak, as they are the most visible of all the peaks. There are some other peaks as well, but they have a very bad signal-to-noise ratio.
We integrate the peaks as described in Section 6.1 and plot the population size versus trap pressure. We find that all the populations show a linear relationship between pressure and intensity. We fit a linear function to the data using weighted linear regression and produce below the resulting fit parameters in table 3.
All of the populations show different slopes and different intersections with the y-axis. The starting point at 1.25×10^{-8}mbar is similar for carbon and oxygen but then shows a great difference in slope. The starting point of CH_2^+ is smaller than the other peaks. This is probably because it is a molecule and dissociates into other smaller molecules, like we discussed in Section 6.2.1, limiting the peak height. The atomic peaks are much larger than the peak of CH_2^+ because they do not dissociate further. This is also evidence for the 1/16 peak being composed of a lot of ionized oxygen.

The 1/16 peak rises with an increase in trap pressure. If the amount of oxygen in the trap were constant and the peak would be solely composed of oxygen, it should stay constant if one increases the injection pressure.
One option for what happens here is that the peak is composed of oxygen and methane, and the injection also contains oxygen. As we take precautions to keep the injection free of oxygen, this is unlikely.
A more likely scenario looks like this: There is oxygen in the trap as well as CH_4^+. Like we discussed in Section 6.2.1 these ions share the same peak in the TOF spectrum. The amount of oxygen in the trap is approximately constant, but upon injecting methane, the methane is added to the peak intensity.
Even though we have a lot of oxygen in the trap, giving the total intensity of the peak some ambiguity as to its composition, one can assume that all the increase we observe with increasing the pressure is associated with an increase in CH_4^+ ions.

The behavior of the peaks is well described as linear in the pressure regime we measured.
By increasing the pressure, we increase the amount of neutral CH_4 in the trap. As the methane gas is of low density, it may be approximated as an ideal gas. Thus, we can use the ideal gas equation to describe it:

$$p_{\text{Trap}} V = n k_B T \tag{50}$$

where p_{Trap} is the trap pressure, V is the volume of the vacuum chamber surrounding the trap, n is the particle density, k_B is Boltzmann's constant, and T is the temperature of the neutral gas.
We vary the trap pressure p_{Trap}, the volume of the vacuum chamber is constant, as well as the temperature of the neutral gas T. Because of this, there is a linear relationship between the trap pressure and the particle density in the trap:

$$n \propto p_{\text{Trap}} \tag{51}$$

The rate of an interaction is proportional to the number of particles involved in the interaction and the corresponding cross section (see section 5):

$$P_{\text{interaction}} \propto n_i \sigma_i \tag{52}$$

As we just stated the number of neutral methane is proportional to the trap pressure, so we find:

$$P_{\text{interaction}} \propto p_{Trap} \tag{53}$$

The interactions here are all reactions that are related to neutral methane.

We can now use the model we described in Section 5 to give a prediction for how the populations change with varying pressure. For this, we can vary the amount of CH_4 in the model. As we used 1 as the starting point in the model and roughly doubled the pressure over the measurement, we will vary the amount of CH_4 from 1 to 2 with steps of 0.1 at an energy of 28 eV, which is also the energy we used for the data, and plot the population sizes against CH_4.
Figure 24 shows how the ion populations change with an increase in neutral methane in the context of the model.
The starting points of the populations is different in the model. While C^+ and O^+/CH_4^+ are at the same height in the data, they are not in the model. This is

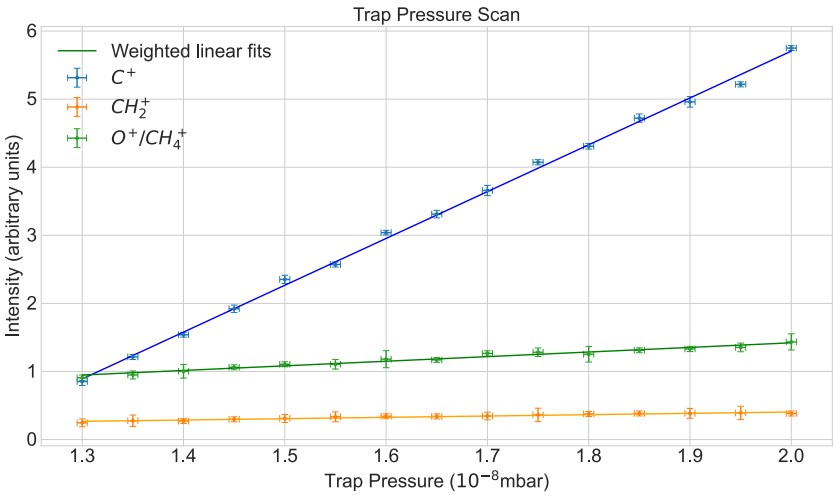

Figure 23: Ion population vs. trap pressure. Error in x-direction are average pressure fluctuations, the error in y-direction: standard error of the mean. The fit was done using weighted linear regression.

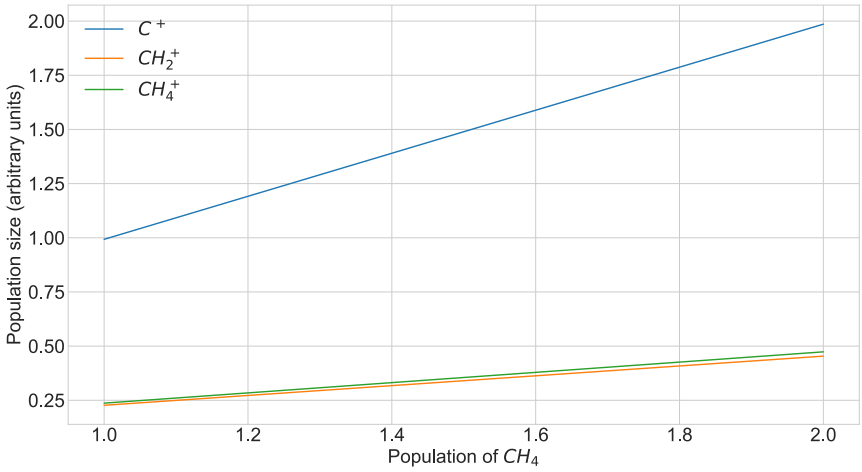

Figure 24: Model population size vs. number of neutral methane in the trap.

because we don't consider the presence of O^+ in the model, which increases the initial height of the 1/16 peak, thus increasing the starting point of CH_4^+.
To compare the model to the data we calculate the ratios of the slopes of the graphs. The slopes of the model are different from the data. While C^+ rises around 34 times faster than CH_2^+ and 10 times faster than CH_4^+ in the data, it only rises around 4 times as fast as CH_2^+ and CH_4^+. Also, the slopes of the molecules are very similar in the model and different in the data.
The data implies that the population of CH_2^+ is overrepresented in our model. It is very close to the population of CH_4^+, and thus their slopes are similar. The reason for this lies in the differential equation describing CH_2^+'s population. We don't consider processes with a small cross-section. Many of these are recombination processes that add to the loss of CH_2^+. If one adds many of these small processes, they may lead to significant losses in the CH_2^+ population and thus change its starting point and slope.
Additionally, we don't consider all the physics that is happening in the trap. One

Table 3: Slopes of the model and data

Ion	Model	Data $(10^{-8}\text{mbar})^{-1}$
C^+	9.92×10^{-3}	6.878(85)
CH_4^+	2.37×10^{-3}	0.676(37)
CH_2^+	2.27×10^{-3}	0.196(18)

potentially important effect may be how ions behave in a filled trap. If the ion populations have built up in the trap, it may favor ions of a "stable" kind like C^+, which cannot dissociate further, or CH_4^+, which is readily produced by the ionization of the neutral gas. CH_2^+, on the other hand, may be less likely to accumulate in a full trap as it dissociates quickly to smaller fragments and is not produced as readily by the ionization of CH_4.

We do observe in the data as well as the model that CH_2^+ shows the smallest slope, followed by CH_4^+ and the largest slope, C^+.
That C^+ has the largest slope can be explained by the fact that it is produced by the total dissociation of methane. If we increase the amount of methane in the trap, there are more ions that can be dissociated into C^+. This is a similar argument to the one we used in Section 6.2.1. As molecular ions have the option of dissociating, their intensity is limited to a greater degree than that of atomic ions. Once they have dissociated far enough down to carbon, there is no further dissociation possible, and the atomic ions may start to build up quicker.

We now discuss why the peak of O^+/CH_4^+ should increase more rapidly than CH_2^+. Like we stated above, the slope of the O^+/CH_4^+ is associated with an increase in the amount of CH_4 in the trap. Because we don't change the energy of the electron beam, we do not expect any changes in the cross sections of the individual processes of dissociation or ionization, as they are not dependent on the number of particles. The probability of an interaction taking place is, however, dependent on the number of particles. It is proportional to the product of the cross section and the number of particles of a given ion. The dynamic that ensues from a larger starting population of methane is not obvious, as feedback loops are involved.
The only reaction that adds to the population of CH_4^+ is the ionization of neutral CH_4. On the other hand, there are multiple processes that add to CH_2^+.
The following conclusion can be drawn: An increase in neutral methane leads to a disproportionate production of CH_4^+ compared to CH_2^+, as the populations of ions that are involved in the production of CH_2^+ do not increase as quickly as the population of neutral methane. This is logical, as the ion populations that lead to the production of CH_2^+ are produced from neutral methane but are also affected by losses.
All the populations that lead to the production of CH_2^+ are CH_4, CH_4^+, and CH_3^+. While all of these populations are increasing with more neutral methane, their losses are also increasing. The loss of neutral methane is not increasing, on the other hand. This leads to the difference in slope that we observe in the model as well as in the data.

6.4 Trap depth

The trap depth is an important parameter to optimize for a good signal-to-noise ratio.
Other works have looked at the optimization of this parameter and have found that there is a maximum at a trap depth of around three to eight volts [19].
However, most of these measurements were done at high energies of the order of 1 keV. We want to find the optimal trap depth for low energies and compare it to the results other authors have found.
We inject methane and measure the TOF spectrum while varying the trap depth. The range of trap depths is $0V$ to $30V$ with steps of $0.1V$. As mentioned in 3.2, we used an asymmetric trap for this measurement. We numerically integrated the peaks of C^+, CH^+, CH_2^+, CH_3^+, and CH_4^+.
We did this measurement immediately after the energy scan of methane that we described in Section 4 and analyzed in Section 6.2.1, where we concluded that the influence of oxygen ions is very limited in this measurement. The same holds true for this set of data.
One can see that the population sizes of the different ions all start at a similar point but change very differently once the trap depth is increased. They all reach a maximum at around 4 to 6V and are almost at baseline again at 20 volts, with the exception of C^+, which is still significantly higher than at baseline.
First, we want to discuss the maximum of the data. One may suspect that a deeper trap may lead to stronger axial confinement of the ions, thus increasing the number of ions in the trap. However, not only is the signal not larger for deeper traps, but the maximum is reached at a rather shallow trap depth.

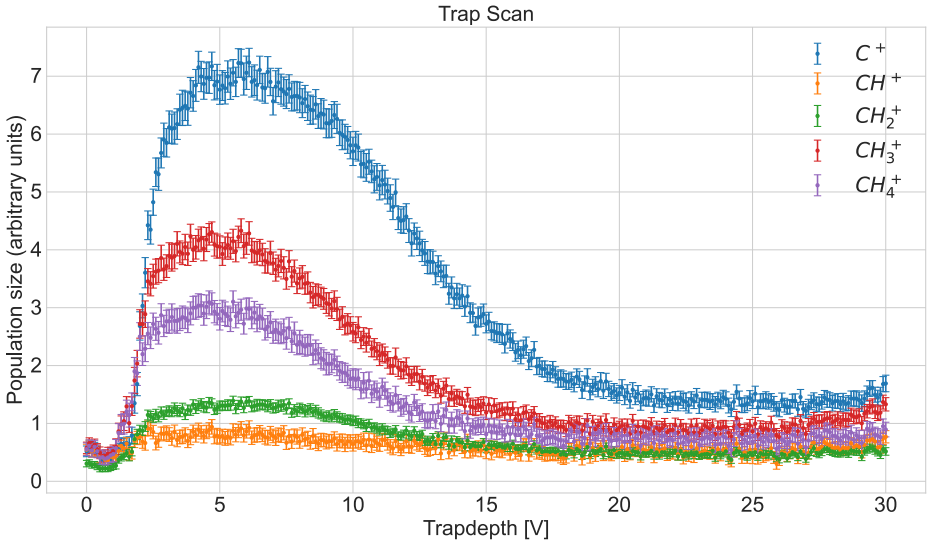

Figure 25: Population size vs trap depth. Errors are the standard error of the mean

A common explanation[20] is connected to equation 54, which relates the trap depth and the ion temperature[18]:

$$k_B T_i \propto q_i V_T \tag{54}$$

A deeper trap leads to more ions being trapped but also to a higher ion temperature. This changes the temperature distribution and can lead to higher evaporative losses.

Thus, more ions escape than are additionally trapped by increasing the trap depth. To understand why different populations are found at different sizes, we can once again compare the data to our model. We use the model shown in Figure 16 at 39.5 eV, which is the energy we used for the trap scan, and compare their relative population sizes (Figure 26).

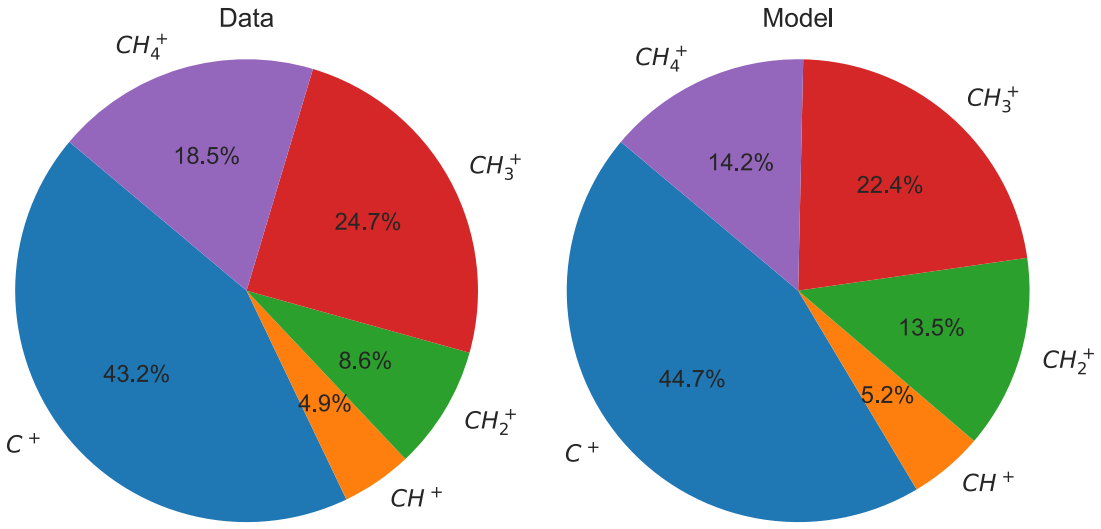

Figure 26: Pie chart comparing the relative ion populations at 39.5eV. Left: Data, Right: Model

The populations follow roughly the same pattern as the data. Like we discussed, CH_2^+ is overrepresented in the model. The populations of CH_3^+, CH_2^+, and C^+ agree well with the data, while CH_4^+ is underrepresented.
If there was a constant amount of gas in the trap, we would find very few ionized molecules, as they would eventually all dissociate into carbon and hydrogen. The main reason we do observe ionized molecules in the trap is that there is a constant flow of neutral gas toward the trap. Thus, new molecular ions can be produced.

Of the molecular ions CH_3^+ is the largest. This is because it has a large cross section for the dissociative ionization from neutral methane but also gains from the population of CH_4^+, while CH_4^+ can only gain from neutral methane and no other ion population.
The most influence by far is shown by the C^+ peak. This can again be explained by the dissociation chain of methane. Carbon is the end product of the dissociation chain of methane. The closer the trap gets to its maximum entrapment of ions, the more methane ions and their associated dissociation products will be present in the trap, leading to more dissociations ending in C^+. This explains the disproportionate influence that trap depth has on the size of the C^+ population.
The differences between the data and the model are also associated with the way we measure the ions. Because we optimize for one ion population, all ion populations are extracted at a slightly different efficiency, leading to a different population distribution than we would expect.

6.5 Breeding time

We are interested in the dependence of the ion's population size on the breeding time, which is the duration that the electron beam interacts with the ions before we

accelerate the ions to the channeltron.
We varied the breeding time between $0.001s$ and $0.13s$ with a step size of $0.0001s$ like described in Section 4 and plotted the ion population size against it in Figure 27 .This measurement was done using a symmetric trap. From the analysis, we excluded the peak of CH^+ as it shows a low signal-to-noise ratio and is located in the ringdown of C^+.

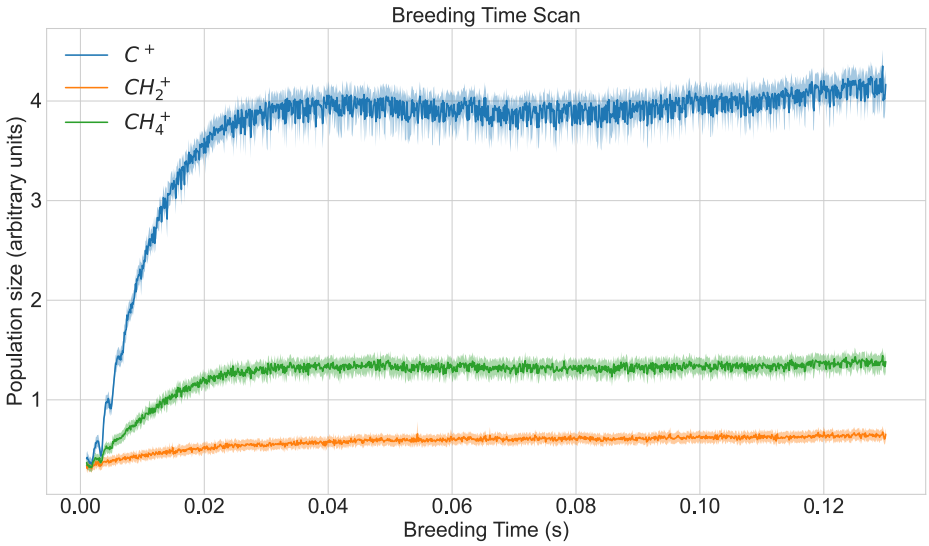

Figure 27: Population size of ions vs. breeding time. The bands around the plots indicate the standard error of the mean.

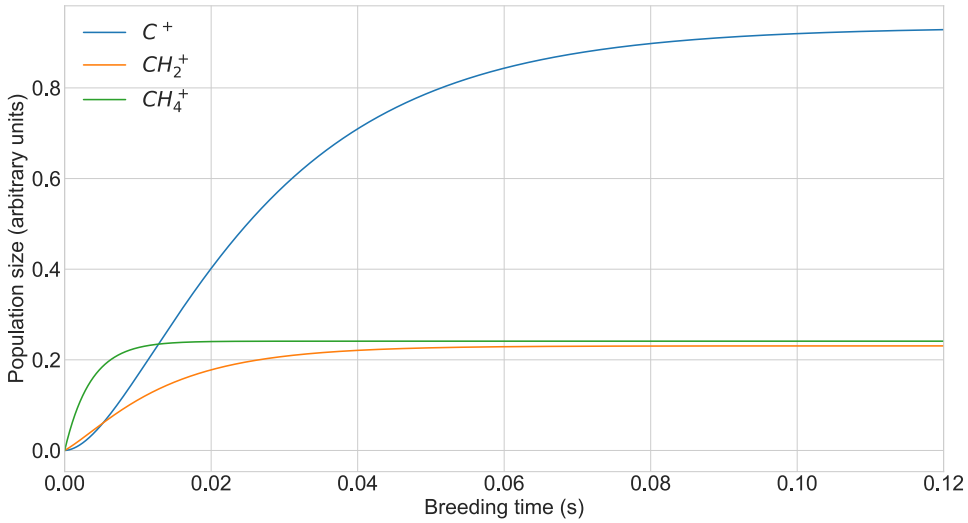

Figure 28: Breeding time model. Equilibrium is reach at different points than in data.

As one can see from Figure 27, all the peaks behave similarly.
At first, they rise quickly until they reach a stable point at around 0.024 s of breeding time. After this point, they still continue to rise slightly, but not much compared to the beginning of the measurement.
The breeding time is the duration that the electron beam interacts with the ion cloud. The lower the interaction time, the lower the likelihood of an interaction

taking place, and consequently, the fewer ions will be produced. When the time of interaction is increased, there is more time for the interaction to take place, and thus more ions are being produced.
Our model gives a prediction for the time evolution of different ion populations. This is shown in Figure 28.
The ratios in equilibrium are similar to those we discussed in the previous section(see 6.4). The time after which equilibrium is reached slightly differs from what we observed in the data. In the model, it is around 0.01 s for CH_4^+, 0.03 s for CH_2^+, and 0.1 s for CH_4^+, while it is 0.024 s for all populations in the data. To understand why this is the case, one first has to understand why the ion populations reach equilibrium in the first place.
An equilibrium is reached because of the way the differential equations describing the growth of an ion's population behave in relation to the population of the ion. The losses of an ion's population are proportional to its own population, while the gains are proportional to the populations of the other ions. This means that when an ion grows while the other populations stay constant, it will reach a point where the losses are as large as the gains. This is the point of equilibrium. The easiest example is CH_4^+. It only gains from the ionization of neutral methane, and its only losses are proportional to its own population size:

$$\frac{dn_{CH_4^+}}{dt} = \frac{e}{j}\left[n_{CH_4}\sigma_{CH_4\to CH_4^+} - \left(n_{CH_4^+}\sum \sigma_{CH_4^+\to CH_x^{+y}}\right)\right] \tag{55}$$

where the sum is the sum of all reactions that remove ions from CH_4^+, these losses also includes radiative recombination and evaporative cooling. If we want to find the population size of CH_4^+ where equilibrium is reached ($\frac{dn_{CH_4^+}}{dt} = 0$), we can rearrange equation 55 to find:

$$n_{CH_4^+,\text{equilibrium}} = n_{CH_4}\frac{\sigma_{CH_4\to CH_4^+}}{\sum \sigma_{CH_4^+\to CH_x^{+y}}} \tag{56}$$

Since the ratio of the cross sections in equation 56 is smaller than 1, CH_4^+ will reach equilibrium at a population size smaller than CH_4. A similar population size can be calculated for every ion.
The time it takes a population to reach this point is dependent on the rate at which the population increases. In the data, the populations all reach the point of equilibrium around the same time because their rate of growth per equilibrium population size is similar. In our model, on the other hand, the populations reach the point at different times. If we take C^+ for example, this is because it has a large equilibrium population but a relatively small rate of growth compared to that. CH_4^+, on the other hand, has a small equilibrium population with a larger growth rate relative to it.
In the model, CH_2^+ is almost as large as CH_4^+, while the data shows a big difference in the populations. It seems that the way we consider CH_2^+ in the model leads to an overrepresentation. The reasons for this were already discussed in Section 6.3: We underestimate the effect of multiple small recombinatory processes and don't consider a potential bias towards certain ions when the trap is full.

6.6 Methane energy scan

The cross-section of the different processes that occur in the EBIT changes with the energy of the electron beam. To study this influence on the spectrum, we varied the

energy of the electron beam while measuring the TOF spectrum. We described the measurement procedure in Section 4.
For the data analysis, we chose to focus on the peaks associated with the ions of carbon and the singly ionized fragments of methane and methane itself (see Figure 17). This almost includes all of the spectrum's peaks only excluding more highly charged fragments of methane as their peaks don't resemble a gaussian very well, indicating that their extraction leaves much to be desired for; thus it is hard to give this signal much meaningfulness.

6.6.1 Correction of the ringdown

As some of the peaks of the TOF spectrum are located below zero because of the ringdown of an earlier peak, their true population size will be smaller when we integrate them without correction. It is necessary to correct the peaks of the methane fragments for the ringdown (see section 8) to get an accurate representation of their population.
Like we described in Section 8, this ringdown can be approximated by the convolution of an exponential decay and a gaussian curve. The smaller the peak intensity, the smaller the following ringdown.

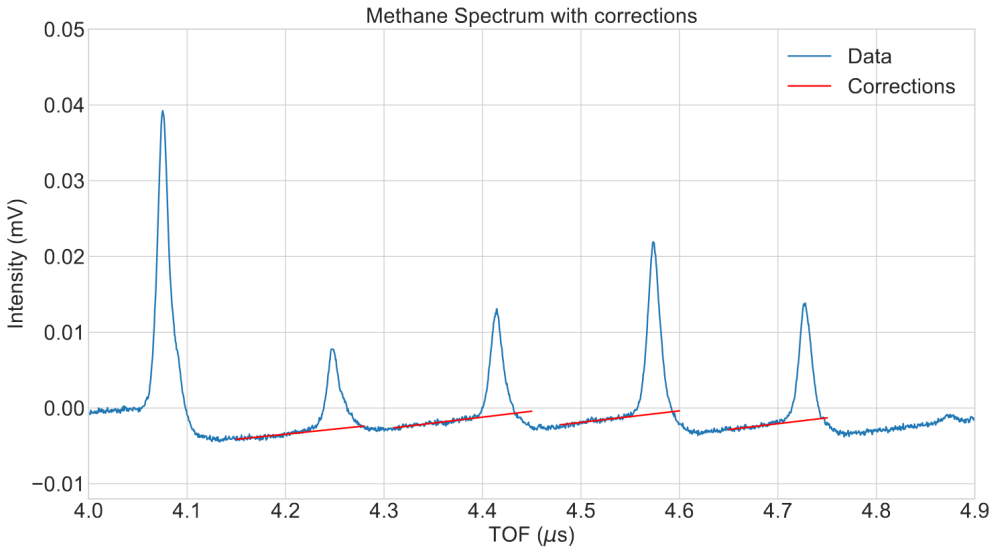

Figure 29: Peaks of the methane spectrum that are corrected for the ringdown. Peaks in the middle are below zero because of the ringdown of the C^+ peak located at the left hand side of the spectrum. Red: Fitted polynomial used for the correction.

One way of correcting this data would be to take equation 29 and fit it to the data to determine the relevant parameters for the function, and then subtract this fitted function from the spectrum.
This would, in theory, be the most sophisticated way of correcting the data. However, during the data analysis, we experienced issues with this method. Firstly, there are many parameters to be determined during the fitting of the function, leading to long computation times and making the fit very error-prone as it often assumes unrealistic values for the fitting parameters, leading to bad fits.
Secondly, and maybe more importantly, because the following peaks are in the ringdown of other peaks, the ringdown signal is difficult to include in the array for the

fitting as it is not purely the convolution we described but rather the convolution plus the following peaks, making the fitting of the complete ringdown almost impossible in many cases.
Another idea for the correction of the data that did not work is to use a corrective array. This is based on the idea that the gaussian peak and ringdown potentially have a regular shape that can be scaled up and down to other peaks. Practically, one would take the shape of one reference peak and ringdown and just scale it up and down to correct the ringdown of other peaks. For scaling, one would use the integral of the peak, as it is proportional to the total charge deposited.
We found this method to have some issues as well, as the shape of the signal was not regular enough to be fitted to other peaks easily. There were significant differences in the shape of the ringdown relative to the peak for each peak that we tried to correct.
After these attempts, we settled on a more pragmatic method that has some advantages over the previous methods as well.
The ringdown in the methane spectrum is sufficiently long so that one can assume the ringdown to be linear during the short time it intersects with the next peak.
We will use around 100 data points before the emergence of a peak to fit a linear approximation of the ringdown. This linear fit will then be subtracted from the corresponding peak. This produces a small error in the correction, as the ringdown is not exactly linear in the region, but it is linear enough to be very close to the real corrected value. The error that is thus produced is very small compared to the statistical error that we assign the data through the process of averaging (see section 6.1).
This method has the advantage that one does not have to make corrections in the order of the peaks. When fitting the exact ringdown function, one has to first correct the ringdown of the carbon peak, then take this corrected spectrum and correct it for the peak of CH^+ and continue ion by ion, as the ringdowns are overlapping.
With the method we are using, however, all the relevant ringdowns affecting a peak will be considered by the linear fit, as the total ringdown will appear as a superposition of all the previous ringdowns. This means we can simply correct every peak by the linear behavior before it and have considered all the relevant ringdown effects.
Figure 29 shows how we fit the linear polynomials to the data. Consider here that we only correct the peaks themselves and not the whole spectrum, as the parts between the peaks are not of interest to us.
We will now integrate the peaks like we have already done before and display them below.

Interpretation of the data

It makes sense to look at all of the populations simultaneously to be able to compare the change in the ion populations with one another.
For this, we will not display the error of the individual populations, as it causes the figure to be too cluttered. The average error of each peak is around 10% of its value.
We will analyze this data by comparing it to the model.
Firstly, one can again see that the population size of the atomic ions is much larger than the population size of the molecular ions. This is again explained by the atoms being the end point of the dissociation chain (see section 6.2.1). This is both true for the model and the data.

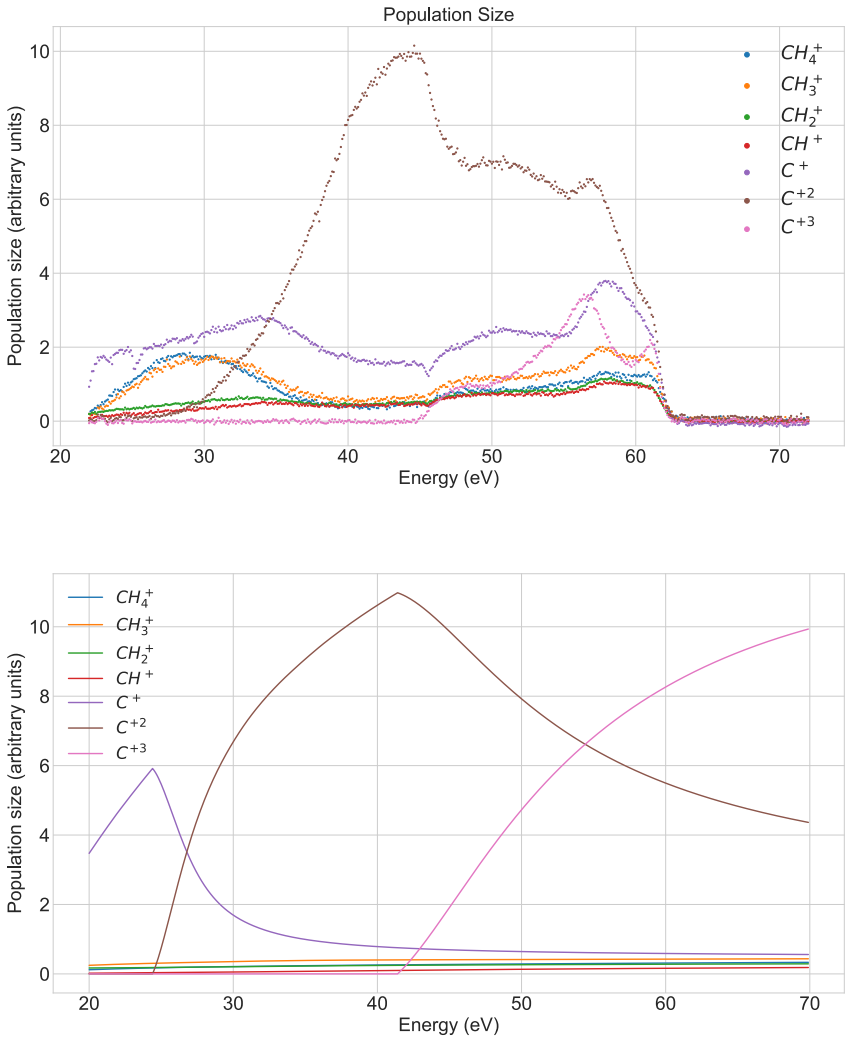

Figure 30: Population size vs. beam energy. Top: Data, Bottom: Model. No error is shown here as the figure would be too cluttered. Similar behavior in carbon ions in both figures.

Many of the large-scale differences in ion population can be traced back to the interaction with carbon ions.
When C^+ is ionized at around 24 eV [12] its population decreases while the population of C^{+2} increases. This point is reached later in the data because we did not consider all reactions that lead to C^+, and thus the point at which the losses are larger than the gains is reached earlier in our model.
The same is true for C^{+2}. It is ionized at around 42 eV [12]. At which point its population decreases while C^{+3} increases. This point occurs slightly later in the data than in the model for similar reasons.

A big difference between the model and the data appears in the population of the molecules. In the model, the populations do not vary much, while in the data, they show big changes. This is especially clear for small energies between 22 eV and 35 eV. In the data, the populations of CH_4^+ and CH_3^+ are noticeably larger than the populations of CH_2^+ and CH^+. Again, CH_2^+ is overrepresented in the model, which may also influence how much CH^+ is present. This could explain this difference.

Another interesting difference appears at around 35 eV. All ion populations begin to decrease as the population of C^{+2} increases. Our model only predicts the decrease of C^{+}. This simultaneous decrease of the molecular ions and increase in C^{+2} may not be related.
However, it could imply that there is a process that leads from molecular ions to C^{+2} that appears around this energy. Given the tables in the appendix, there is exactly such a mechanism that we included in the model.
Below the energy of 30 eV, only dissociative excitation and electron impact ionization of neutral methane may happen. All of these processes have a low cross section toward the production of C^{+}. This makes up only about 5% of the total cross section. It follows that the cross section toward the production of C^{+2} must be lower than 5% of the total cross section of these processes. However, beginning at around 34 eV, there is the process of dissociative ionization from ionized molecules to C^{+}, which has a much larger relative cross section of 20% and up to 45% of the total cross section. This adds to the total production of C^{+}, which in turn may be ionized to C^{+2}. This is not a direct pathway to C^{+2} but rather a two-step process leading over C^{+}. One can see a representation of this mechanism in Figure 31

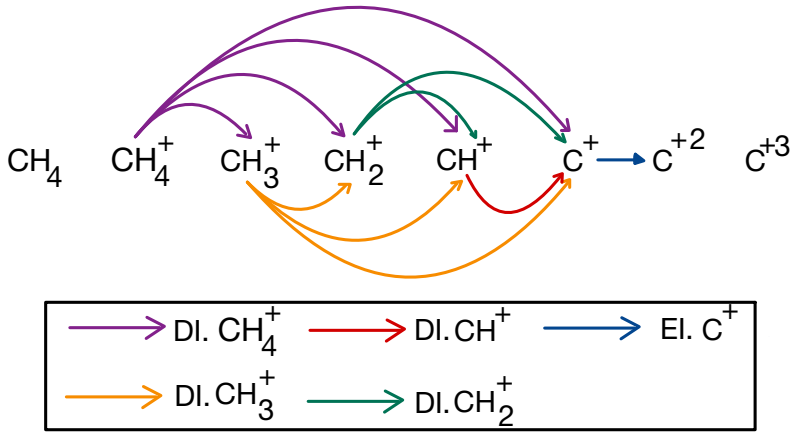

Figure 31: Scheme of the proposed mechanism potentially explaining the decrease of the molecular ions at around 35 eV. Shown are the processes of dissociative ionization leading to C^{+} which in-turn is ionized to C^{+2}.

Yet, we considered this mechanism in the model and did not see any changes. This may be because, in reality, the trap biases towards carbon ions as they cannot dissociate. The trap has a certain capacity for trapping ions. After it has reached its limit, there may be some bias toward more 'stable' ions, meaning less chance of dissociation. This would lead to a larger accumulation of carbon ions and would also increase the effect of the mechanism leading from ionized molecules to C^{+2}.

The last big difference is found at higher energies between 45 eV and 60 eV. The model only predicts the rise of C^{+3} and the decrease of C^{+2}. In the data, one finds that the molecular ions and carbon rise as well in this regime. In our model, we have no processes relating to the molecular ions, or C^{+} that arise at this energy. Especially those that increase these populations.

If one just considers the molecular ion populations and C^+, one can see that they all behave very similarly in the data. This looks more like a global effect than individual cross-sectional changes. This global effect is shown in Figure 32.

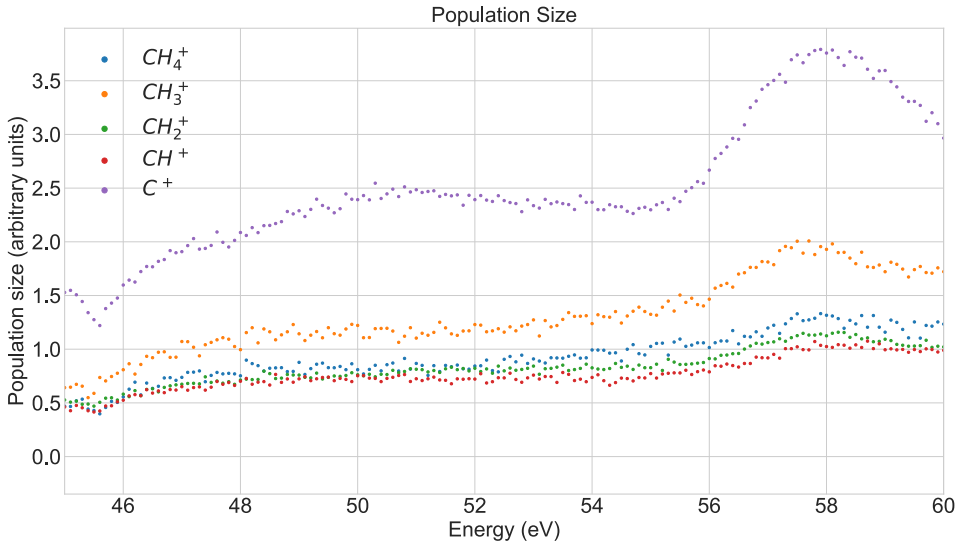

Figure 32: Molecular ion populations and C^+ vs. beam energy. All populations show similar behaviour in this energy region, leading back to changes in the extraction efficiency.

This may occur because the extraction efficiency changes with increasing energy. Upon increasing the energy, the space charge of the trap changes. This leads to a change in the effective kick voltage that the ions experience. Thus, they are extracted differently and potentially more efficiently. This coincides with the appearance of C^{+3}. As this ion population appears, the space charge changes quickly, thus leading to a abrupt change in the extraction for every ion.

Another interesting observation is that the population of C^{+2} is the largest population in the data as well as in the model. C^{+3} is also very large in the model, but this is due to the fact that the only mechanisms causing losses for C^{+3} are evaporation and radiative recombination.
In our discussion of the model in Section 5, we showed that the population of C^{+2} does not converge for the breeding times we chose in the experiment. We did not measure the population of C^{+2} as a function of breeding time, which makes us unable to confirm that this is the case in the experiment. However, if this were true, it would imply that the potential population of C^{+2} may be much larger for larger breeding times, and we extract this population while it is still not in a state of equilibrium.
The reason this population is so large lies in the fact that it gains from the C^+ population, which is the end of the dissociation chain, while only losing to C^{+3} at higher energies.
Past 60 eV, all the populations go to zero. This is not because we stop producing ions in the trap but rather because it is associated with the asymmetric trap. For this measurement, we used an asymmetric trap where DT3 is at roughly 60V potential and DT5 is 6V higher than DT4. When the potential of DT4 is increased, the trap becomes less asymmetric and eventually becomes a symmetric trap when DT4 is at

54V. After this point, the trap is asymmetric in the other direction, and extraction becomes exceedingly hard. We never quite reached a potential of 54V, but the measurement indicates that the asymmetry of the trap was sufficiently disturbed by the increase in potential of DT4, such that the extraction efficiency dropped very rapidly.

6.7 Disappearance of the signal at low energies

During the measurements, we noticed that the signal is lost very reliably at beam energies of around 15 eV. We want to study this more carefully to better understand what limits our ability to lower the energy further. Like we stated in Section 4, we did a measurement where we lowered the energy until the spectrum disappeared. Below is the spectrum during the three steps of this process, where the spectrum shows a good, medium, and eventually very bad signal-to-noise ratio.

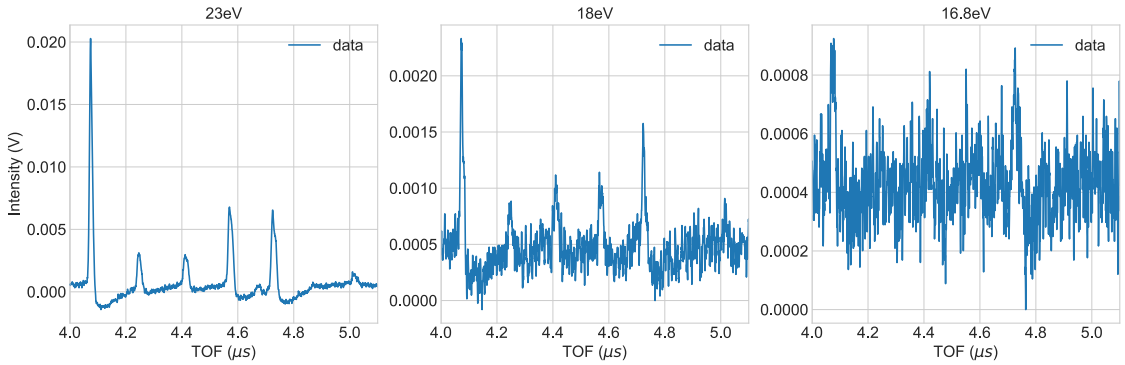

Figure 33: Three spectra of the disappearance measurement. First spectrum: clearly visible peaks, second spectrum: signal to noise ratio is small but peaks are still visible. Right plot: peaks are barely visible as the noise grows.

In the first figure, one can clearly see all the peaks of methane's dissociation products we identified in Section 6.2.1. This measurement was taken shortly after the energy scan for methane. We concluded in Section 6.2.1 that the influence of O^+ on the CH_4^+ peak is negligible. The same is true for this measurement. In the second figure, one can see that the signal-to-noise ratio has worsened while all of the peaks are still visible. The last figure shows the signal after the spectrum has disappeared. It is just composed of noise.
If we integrate over the peaks like we described in Section 6.1, we can display how the intensity changes with lower energies. As the signal-to-noise ratio gets worse the lower the beam energy, the statistical error from averaging is naturally very large in this measurement. We will not show the error in the figure with all graphs to increase visibility. However, we show two of the populations in figure 34 to give an idea of how large the errors are.
The intensity of all the peaks decreases continuously without sudden drops in intensity. This implies that there is no resonant process that leads to the disappearance of the spectrum, but rather that the loss of the signal is associated with a global worsening of the production and extraction of the ions.
To understand where the theoretical limit of the signal lies, it is worth considering the tables provided in the appendix. These tables give all the pathways of dissociation of methane we considered in the model. Especially important here is the following process:

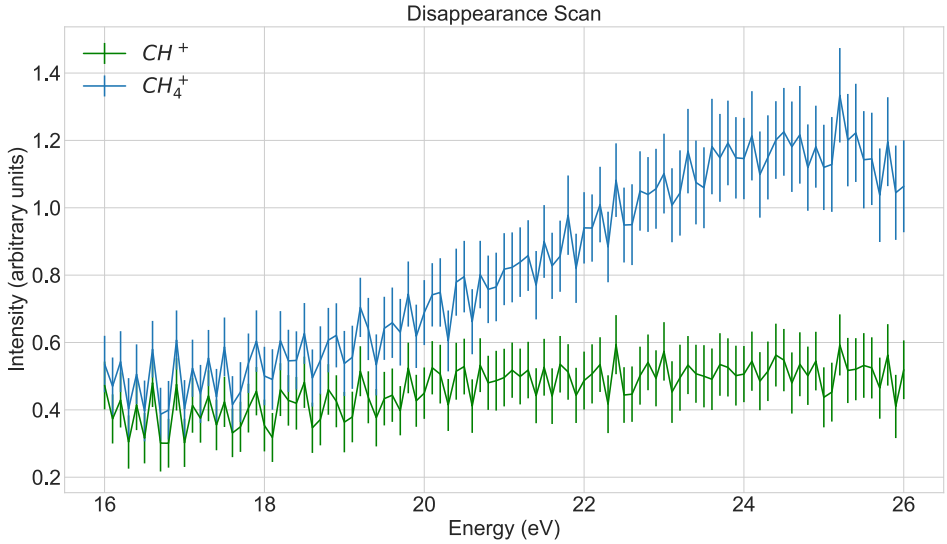

Figure 34: Two of the total five graphs with errors. Error is the standard error of the mean.

$$e + \mathrm{CH_4} \rightarrow \mathrm{CH_4^+} + 2e \tag{57}$$

This process is only possible at energies larger than 12.6 eV (see appendix). It is the process of electron-impact ionization of neutral methane. This is the basis for the further dissociation of other ions. If the electron energy is lower than this energy, no ions can be produced from methane. The threshold energies for neutral dissociation of methane are at lower energies, but we assume that neutrals are not trapped and can thus not contribute to an ion population. Thus, this describes the theoretical limit of how low we can choose the beam energy and still see the spectrum of the dissociation products of methane.
As the spectrum disappears at an energy of roughly 17 eV, we are only 4.4 eV away from the theoretical limit. Effects like negative space charge may also play a role in further lowering the true electron energy (see Section 3.4.2). Meaning, it is possible that we are even closer to the theoretical limit.

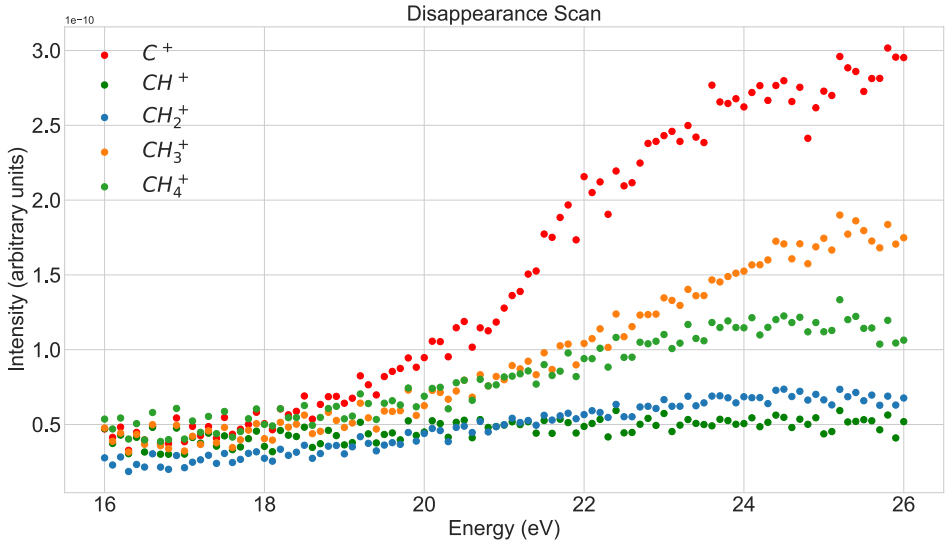

Figure 35: Population size as a function of beam energy. Errors have been excluded for better visibility.

7 Conclusion and outlook

The goal of this thesis was to understand how methane is ionized and dissociated in an EBIT at low energies.
A key idea to make this possible was to use the integral of the peaks in the TOF data as a measure for an ion's population. The fluctuations of the spectrum were one of the main sources of error in the experiment.

To interpret the data, we created a model that considered the rates at which different ion populations increase and decrease. These were formulated as coupled differential equations that were solved using the Runge-Kutta method.

We took TOF spectra of methane and ethane to identify what ions are present in the trap.
To identify the lines correctly, we provided evidence of different kinds. Our previous knowledge of what molecules are possibly present helped in formulating a guess for a TOF calibration.
We were able to differentiate atomic peaks from molecular peaks as they are not as limited in their intensity by dissociation.
The ionization energies of the atoms present in the trap were used to identify the ions of carbon and prove that very little water was in the trap, as no oxygen peaks were present.
Doubly ionized fragments of ethane were found in the spectrum of ethane, which was surprising to us, as we suspected the molecules to dissociate before reaching a state of double ionization.
This proved that it is possible to ionize molecules with an EBIT without completely dissociating them.

We determined optimal experimental parameters to increase the signal, which is naturally very low at the energies we operated the EBIT at.
We varied the pressure while measuring the ion populations to find the optimum of this parameter. All ions showed a linear relationship between population size and

pressure, while the slopes were different for every ion. The slopes were compared to the slopes predicted by the model for an increase in neutral methane. The model was able to predict the ordering of the slopes from largest to smallest. It showed similar slope ratios for the slope of CH_4^+/CH_2^+, while the ratio of C^+/CH_4^+ and C^+/CH_2^+ were smaller in the model than in the data. The reason for this is that the model does not consider all reactions leading to C^+ thus this slope is underrepresented.
The linear growth was predicted by our model as a consequence of the neutral methane population being an ideal gas and the temperature and volume remaining constant.
We also discussed the difference in slope between CH_4^+ and CH_2^+ and traced it back to the fact that CH_2^+ is produced by other molecular ions that suffer from losses, while CH_4^+ is only produced from neutral methane, which does not lose any particles as there is constant replenishment.

The optimal trap depth interval is between four and six volts of trap depth on one side of an asymmetric trap. The other side was at a potential of 60V.
This finding proved to be similar to what other works also found [19, 20]. It was explained by ion temperatures rising with deeper traps, leading to more losses than ions gained by the deeper trap.
Here, the model was used to predict the share of an ion's population in the total ion count. We found that CH_2^+ is overrepresented in the data due to not considering neutral processes in the model, while the other populations were well predicted by the model, with the exception of CH_4^+.

The breeding time was shown to have a great influence on the ion population. At first, populations rise quickly with breeding time. Eventually, a state of equilibrium is reached after 0.024 s. This point was similarly predicted by our model for the molecular ions, although there were some differences. The equilibrium is established as a consequence of population-dependent losses that increase until the losses are as large as the gains from other ion species.
The model did not predict the time of equilibrium for the C^+ population, again because the model does not include all possible reactions.

We planned on measuring the influence of the current on the ion population size. However, a systematic error was made that led to the energy being varied in parallel to the current.
It would be interesting to repeat this measurement without this error to better understand how the current influences the ion population. For this particular experiment, it was not necessary to determine an ideal value for the current, as the current was constantly very low due to losses in transmission through the off-axis electron gun. Because of this, we aimed for as large a current as possible in every measurement.

To better understand the interactions between the ions, we measured the ion populations while varying the electron beam energy.
To get a more accurate representation of the ion populations, we corrected for the ringdown.
Our model was able to explain many of the structures we observed, indicating that the changes in population arise due to changes in cross-section that dictate how ion populations interact with each other.
The model did not predict the drop of the molecular ions around 35 eV electron beam energy. We provided an explanation for this behavior in discussing the influence of

dissociative ionization. While we included this in our model, it may not show because of different effects concerning the trap physics that we did not consider.
The rise at around 45 eV was explained as a global effect, due to changes in the extraction efficiency.
The drop off at 60 eV is due to the trapping being disturbed by the asymmetry of the trap decreasing.
We were able to explain most of the behavior of the carbon ions. The model was also able to predict the sequence of the molecular ions' populations.

Finally, we measured the point of disappearance of the ions. It showed that we lose the signal completely at an energy of 17.1 eV, which is 4.4 eV above the theoretical limit for ionization of neutral methane.
This shows that an EBIT can be used to produce ionized molecules at very low energies.

This work may be improved by using an on-axis electron gun instead of the off-axis version we used. For these measurements, the off-axis gun was mostly a disadvantage, as it caused the transmission and thus the current to be very low. This made the signal-to-noise ratio worse than if we had used an on-axis gun.
Another improvement may be made by optimizing the TOF spectrum for C^+ instead of CH_3^+. This would have made the comparison to the model more accurate.
The model can be improved by including all reactions between the ions, no matter how small they may be, as it is difficult to say how large this affects the dynamics of the ions. Additionally, one could also include effects like dielectronic recombination [19] and charge exchange. These may be able to predict smaller structures in the data.
It may also be interesting to inspect additional molecules, like the polycyclic aromatic hydrocarbons we mentioned in the introduction. All the strengths of the miniature EBIT that make it a well-rounded atomic ion source may be translated to molecular ions. This could provide a novel and potentially superior way of conducting studies in molecular physics. Especially if the EBIT is used in combination with other light sources, such as synchrotron radiation.

References

[1] Moto Togawa. "Investigation of the M-shell unresolved transition array of aluminium-like iron using monochromatic soft x-ray synchrotron radiation". MA thesis. 2021

[2] Lotz, W. "An empirical formula for the electron-impact ionization cross-section". Z. Physik 206, 205–211 (1967). https://doi.org/10.1007/BF01325928

[3] McMurry, J. "Organic Chemistry: A Tenth Edition". OpenStax, 2023, pp. 78-81. ISBN: 978-1-951693-98-5

[4] Reiter, D. and Janev, R.K. (2010), "Hydrocarbon Collision Cross Sections for Magnetic Fusion: The Methane, Ethane and Propane Families". Contrib. Plasma Phys., 50: 986-1013. https://doi.org/10.1002/ctpp.201000090

[5] R. K. Janev and D. Reiter, Phys. Plasmas 9, 4071. 2002.

[6] R. K. Janev and D. Reiter, Phys. Plasmas 11, 780. 2004

[7] P. Micke et al. "The Heidelberg compact electron beam ion traps". In: Review of Scientific Instruments 89.6 (June 2018), p. 063109. doi: 10.1063/1.5026961.

[8] Steffen Kühn. "High-precision soft X-ray transition measurements of neon-like mid-Z ions using ultra monochromatic synchrotron." PhD thesis. 2021

[9] Gabriel Herrmann. "Optical Theory of Thermal Velocity Effects in Cylindrical Electron Beams". In: Journal of Applied Physics 29.2 (Feb. 1958), pp. 127–136. doi: 10.1063/1.1723053.

[10] Jonas Danisch. "Search for the O_{16}^{4+}/O_{18}^{4+} isotope shift in the photoionization of Be-like oxygen with monochromatic soft X-ray synchrotron radiation". BA thesis. 2022

[11] Atkinson, Kendall E. (1989), "An Introduction to Numerical Analysis (2nd ed.)", New York: John Wiley & Sons, pp. 249-263, ISBN 978-0-471-50023-0

[12] A. Kramida et al. NIST Atomic Spectra Database (ver. 5.11), [Online]. Available: https://physics.nist.gov/asd [2016, January 31]. National Institute of Standards and Technology, Gaithersburg, MD. 2023.

[13] D. H. Crandall, J. A. Ray, Carmen Cisneros. "Channeltron efficiency for counting of H+ and H- at low energy." Rev. Sci. Instrum. 1 May 1975; 46 (5): 562–564. https://doi.org/10.1063/1.1134258

[14] Demtröder, W. (o. J.). "Experimentalphysik 3: Atome, moleküle und festkörper", 2010. Springer.

[15] Crespo Lòpez-Urrutia, J. & Harman, Z. (2014, 01). "Emission and laser spectroscopy of trapped highly charged ions in electron beam ion traps". In (Bd. 256, S. 315-373).

[16] Bethe H. Ann. Physik. "Zur Theorie des Durgangs schneller Korpuskularstrahlen durch Materie", 1930;5:325.

[17] D. Reiter, B. Küppers, http://www.hydkin.de (2008).

[18] F. Currell and G. Fussmann, “Physics of electron beam ion traps and sources,” IEEE Transactions on Plasma Science, vol. 33, pp. 1763–1777, 2005. [Online]. Available: https://doi.org/10.1109/TPS.2005.860072

[19] Marleen Maxton. ”Study of dielectronic recombination resonances and their strengths in highly charged oxygen ions”. BA thesis. 2023

[20] P. Beiersdorfer, L. Schweikhard, J. Crespo López-Urrutia, K. Widmann; ”The magnetic trapping mode of an electron beam ion trap: New opportunities for highly charged ion research”. Rev. Sci. Instrum. 1 November 1996; 67 (11): 3818–3826. https://doi.org/10.1063/1.1147276

[21] Valdas Jonauskas, ”Electron-impact double ionization of the carbon atom”, A&A, 620 (2018) A188, DOI: https://doi.org/10.1051/0004-6361/201834303

[22] Steffen Kühn. “High-precision soft X-ray transition measurements of neon-like mid-Z ions using ultra monochromatic synchrotron.” PhD thesis. 2021

[23] D.E. Harris and D. Irwin. Einstein Observatory Revised User’s Manual. Harvard-Smithsonian Center for Astrophysics,. 1984. url: https://heasarc.gsfc.nasa.gov/docs/einstein/RUM_Chapter1-2.pdf.

[24] Frederik B.S. Paerels and Steven M. Kahn. “High-Resolution X-Ray Spectroscopy with Chandra and XMM-Newton.” In: Annual Review of Astronomy and Astrophysics 41.1 (Sept. 2003), pp. 291–342. doi: 10.1146/annurev.astro.41.071601.165952

[25] Maria Santos-Lleo et al. “The first decade of science with Chandra and XMM-Newton”. In: Nature 462.7276 (Dec. 2009), pp. 997–1004. doi: 10.1038/nature08690.

[26] Szczepanski, J., Vala, M. ”Laboratory evidence for ionized polycyclic aromatic hydrocarbons in the interstellar medium”. Nature 363, 699–701 (1993). https://doi.org/10.1038/363699a0

[27] Cartwright, Julyan HE, and Oreste Piro. ”The dynamics of Runge–Kutta methods.” International Journal of Bifurcation and Chaos 2.03 (1992): 427-449.

[28] B. M. Penetrante, M. A. Levine*, J. N. Bardsley; Computer predictions of “evaporative” cooling of highly charged ions in EBIT. AIP Conf. Proc. 1 June 1989; 188 (1): 145–157. https://doi.org/10.1063/1.38413

[29] Ron Parker.”Introduction to Plasma Physics 1”. In: MIT open course ware (2006), Chapter 3. Collisions in plasmas.

[30] G. Y. Liang et al 2009 ApJ 702 838.

[31] W. Quint. ”Fundamental Physics in Particle Traps”, Chapter 10, Springer Tracts in Modern Physics, Volume 256, (2014), ISBN: 978-3-642-45200-0.

[32] Hiroya Suno, Takako Kato, ”Cross section database for carbon atoms and ions: Electron-impact ionization, excitation, and charge exchange in collisions with hydrogen atoms”, Atomic Data and Nuclear Data Tables,Volume 92, Issue 4, 2006, Pages 407-455,ISSN 0092-640X, https://doi.org/10.1016/j.adt.2006.01.001.

Acknowledgements

I want to express my gratitude to Prof. José Crespo for guiding me through this thesis and giving me the opportunity to use the equipment from the MPIK. I also want to thank Marc Botz for helping me get started with the experiment and advising me during the writing of this thesis. Furthermore, I would like to thank Jonas Danisch for helping me with the construction of the model and Joschka Goes for helping me with the implementation of the code for the measurement scheme.

A Processes considered in the model

All the tables were taken from [5]. The reactions for the direct ionization of carbon ions are not listed here, but included in the model.

Reaction		I_p or A_p (eV)	$\overline{E_{\text{el}}^{(-)}}$ (eV)	$\overline{E_K}$ (diss. products) (eV)
$e+CH_4$	$\rightarrow CH_4^+ + 2e$	12.63	12.63	···
	$\rightarrow CH_3^+ + H + 2e$	14.25	17.49	3.2
	$\rightarrow CH_2^+ + H_2 + 2e$	15.1	18.83	3.7
	$\rightarrow CH^+ + H_2 + H + 2e$	19.9	23.5	3.6
	$\rightarrow C^+ + 2H_2 + 2e$	19.6	24.6	5.0
	$\rightarrow H^+ + CH_3 + 2e$	18.0	20.7	3.0
	$\rightarrow H_2^+ + CH_2 + 2e$	20.1	25.6	6.0

Figure 36: Electron impact ionization of neutral methane. I_p appearance energy, $\bar{E}_{el}^{(-)}$ mean electron loss, $\bar{E}_K$ mean total kinetic energy of products. The last two reactions are not considered in the model.

Reaction	Channel	R_{DI}^+	$E_{\text{th}} = \overline{E_{\text{el}}^{(-)}}$ (eV)	$\overline{E_K}$ (ion.prod.) (eV)
$e+CH_4^+$	$\rightarrow e + CH_3^+ + H^+ + e$	0.35	27.05	11.78
	$\rightarrow e + CH_2^+ + H + H^+ + e$	0.24	32.48	11.78
	$\rightarrow e + CH^+ + H_2 + H^+ + e$	0.22	33.09	11.78
	$\rightarrow e + C^+ + H_2 + H + H^+ + e$	0.19	36.76	11.78
$e+CH_3^+$	$\rightarrow e + CH_2^+ + H^+ + e$	0.40	30.81	11.78
	$\rightarrow e + CH^+ + H + H^+ + e$	0.31	35.94	11.78
	$\rightarrow e + C^+ + H_2 + H^+ + e$	0.29	35.09	11.78
$e+CH_2^+$	$\rightarrow e + CH^+ + H^+ + e$	0.55	30.41	11.78
	$\rightarrow e + C^+ + H + H^+ + e$	0.45	34.15	11.78
$e+CH^+$	$\rightarrow e + C^+ + H^+ + e$	1.00	29.0	11.78

Figure 37: Dissociative ionization. R_{DI}^+ branching ratios,E_{th} threshold energy, $\bar{E}_K$ mean total kinetic energy of products. All reactions are considered in the model.

Reaction	Channel	R_{DE}^{+}	$E_{th}=\overline{E}_{el}^{(-)}$ (eV)	$\overline{E}_K$ (products) (eV)
$e+CH_4^+$	$\rightarrow CH_3^+ + H + e$	0.360	5.2	3.6
	$\rightarrow CH_3 + H^+ + e$	0.315	8.0(#)	2.6
	$\rightarrow CH_2^+ + H_2 + e$	0.140	6.5	4.0
	$\rightarrow CH_2 + H_2^+ + e$	0.073	9.5(#)	2.0
	$\rightarrow CH^+ + H_2 + H + e$	0.068	10.0	2.4
	$\rightarrow C^+ + 2H_2 + e$	0.044	10.4	3.7
$e+CH_3^+$	$\rightarrow CH_2^+ + H + e$	0.256	10.6	5.3
	$\rightarrow CH_2 + H^+ + e$	0.515	11.0[a]	2.5
	$\rightarrow CH^+ + H_2 + e$	0.125	12.0	6.1
	$\rightarrow CH + H_2^+ + e$	0.048	11.3[a]	0.8
	$\rightarrow C^+ + H_2 + H + e$	0.056	14.0	4.5
$e+CH_2^+$	$\rightarrow CH^+ + H + e$	0.195	12.0	7.0
	$\rightarrow CH + H^+ + e$	0.675	9.0[a]	2.4
	$\rightarrow C + H + H^+ + e$	0.040	14.2	3.3
	$\rightarrow C^+ + H_2 + e$	0.056	11.0	6.8
	$\rightarrow C + H_2^+ + e$	0.021	11.6[a]	3.3
	$\rightarrow C^+ + 2H + e$	0.013	15.5	6.8
$e+CH^+$	$\rightarrow C^+ + H + e$	0.09	12.2[b]	8.2
	$\rightarrow (CH)^{**} \rightarrow C^+ + H + e$	1.0	2.5	4.0
	$\rightarrow C + H^+ + e$	0.91	5.0[a]	2.0
			$\overline{E}_{el}^{(-)}=8.4$[b]	

Figure 38: Dissociative excitation. R_{DE}^{+} branching ratios, E_{th} threshold energy, $\bar{E}_K$ mean total kinetic energy of products. In the model the first reaction of each ion population is considered to contribute to another ion population. The rest of the reactions are considered to decrease the given ion population without adding to another.